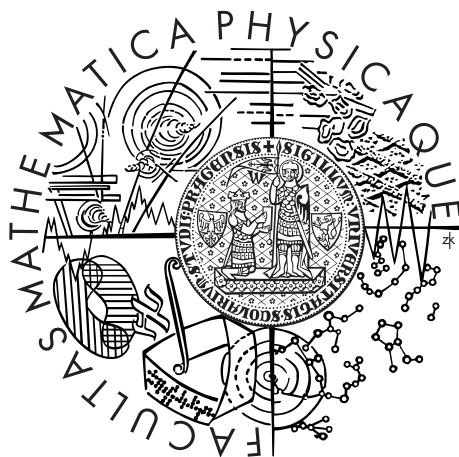Univerzita Karlova v Praze
Matematicko-fyzikální fakulta

DIPLOMOVÁ PRÁCE

Jakub Benda

Účinné průřezy srážek elektronů s atomy vodíku

Ústav teoretické fyziky

Vedoucí práce: RNDr. Karel Houfek, PhD.
Studijní program: Fyzika, Teoretická fyzika

2012

Prohlašuji, že jsem tuto diplomovou práci vypracoval samostatně a výhradně s použitím citovaných pramenů, literatury a dalších odborných zdrojů.

Beru na vědomí, že se na mojí práci vztahují práva a povinnosti vyplývající ze zákona č. 121/2000 Sb., autorského zákona v platném znění, zejména skutečnost, že Univerzita Karlova v Praze má právo na uzavření licenční smlouvy o užití této práce jako školního díla podle § 60 odst. 1 autorského zákona.

V Praze dne

Jakub Benda

Název práce: Účinné průřezy srážek elektronů s atomy vodíku
Autor: Jakub Benda
Katedra (ústav): Ústav teoretické fyziky
Vedoucí bakalářské práce: RNDr. Karel Houfek, PhD.
e-mail vedoucího: karel.houfek@mff.cuni.cz

Abstrakt: Přestože je srážka elektronu s atomárním vodíkem dlouhá desetiletí zkoumaným jevem, stále není k dispozici ani úplná databáze rozptylových dat, ani všeobjímající metoda, která by umožnila taková data generovat. Pro astrofyzikální a další účely jsou nezbytné účinné průřezy elektron-vodíkových srážek v rozsáhlém oboru energií, od desetin elektron-voltu do milionů elektronvoltů. V této práci se autor detailněji věnuje několika rozšířeným přístupům k řešení elektron-atomového rozptylu a srovnává výsledky vlastních implementací těchto metod s publikovanými daty a výsledky volně dostupných počítačových kódů. Překryvům jednotlivých metod je věnována obzvláštní pozornost, tak, aby na konci mohla být nabídnuta databáze s jednoduchým uživatelským rozhraním pro běžné praktické použití rozptylových dat v aplikovaných odvětvích.

Klíčová slova: elektronový rozptyl, atomární vodík, vnější komplexní škálování

Title: Cross sections of collisions of electrons with hydrogen atoms
Author: Jakub Benda
Department: Institute of theoretical physics
Supervisor: RNDr. Karel Houfek, PhD.
Supervisor's e-mail address: karel.houfek@mff.cuni.cz

Abstract: Although the collisions of electrons and atomic hydrogen has been studied for several decades, there is still neither a complete database of scattering data, nor a universal method that would let generate such data. For astronomical and other purposes the cross sections of electron-hydrogen collisions are necessary, in a broad range of energies – from tenths of electronvolt to millions of electronvolts. In this work the author concentrates on several established approaches to electron-atom scattering and confronts results of his own implementations of these methods against the published data and results of freely available computer codes. A special attention is given to the overlaps of different methods, so that in the end a database with easy user interface can be offered for common practical usage of scattering data in applied fields.

Keywords: electron scattering, atomic hydrogen, exterior complex scaling

Contents

Chapter 1

Introduction

Electron-atom scattering processes play an important role in astrophysical phenomena. Stellar atmospheres often happen to be a stage for violent collisions of emitted particles and the omnipresent light-element gas. Likewise, the interstellar medium is constantly ruffled by stellar wind and other sources of accelerated particles. Both events contribute to the dynamics of the participating matter and – moreover – they provide invaluable means of observation.

Most experimental data in astronomy consist of optical measurements, e.g. the spectra of stellar radiation. Such data contain more or less decipherable signature of surface microscopical processes in the form of spectral lines, originating also in de-excitation of previously excited atoms. The original excitation can be achieved in many ways – by exposition to a hard UV radiation, by atom-atom collisions etc., but among them the most important (at least in absence of electromagnetic radiation) are the collisions with free accelerated elementary particles: protons and electrons.

The observed de-excitation radiation can be polarized with a polarization dependent on the direction of both incident and outgoing projectiles. [1] Thus, measuring a polarization degree can offer an insight into the physics of stellar atmosphere including not only its composition, but also the direction and massiveness of atmospherical currents.

The most basic scattering event happening on Sun and other stars is the collision of electrons with hydrogen atoms in the ground state. This thesis focuses on a precise determination of the electron-hydrogen cross sections for elastic processes and for excitation. Such a task involves a discussion of available data, methods, as well as ready-made computer codes. As was shown in [2], there exists a variety of ready computer programs, which compute scattering variables for electron-atom collisions. A confrontation of their results proved that none of them can be used as the final code that would produce all necessary data with a given precision. Even for electron-hydrogen scattering, detailed cross section data are neither freely available nor easily obtainable with present specialized approaches, which are mostly valid in a limited energy range. Successful interpretation of astronomical data, however, requires models which need as an input the cross sections in the broad energy range, from fractions of eV up to several MeVs.

In addition to astrophysics, electron-hydrogen collisions are a cornerstone of plasma physics. As stated in [3], the hydrogen line intensity ratios H_γ/H_α and H_β/H_α serve as density indicators in tokamak physics. These coefficients are greatly dependent on the the impact excitation cross sections from H(1s) to higher quantum levels (to $n = 6$) at high temperatures (~ 10 eV) and also on the "stepwise" cross section between consecutive energy

levels at low energies (~ 0.1 eV).

This thesis arised for the needs of collaborators from the Astronomical Institute, whose research areas involve scattering events in plasmas. Data for several processes are already tabulated in on-line databases, which will be briefly mentioned in chapter 2. The general requirements of atronomers, though, span broader theory and are listed below:

- For modelling various isotropical electron-hydrogen (and proton-hydrogen) collisions the integral cross sections for fine structure transitions H($nljm$)$\rightarrow$H($n'l'j'm'$) are necessary. The main contribution comes from low n's up to the level $n = 3$ and from low energies, mostly up to 10 eV.

- Determining impact polarization in solar flares requires angular distribution of the previous, i.e. the differential cross section, for a wide range of energies from threshold to tens of keVs.

- Depolarization by proton collisions doesn't change the principal quantum number (i.e. transitions will have the scheme H($nljm$)$\rightarrow$H($nl'j'm'$)) and occurs at energies around 1 eV.

- Common transition rates are computed from cross sections integrated with Maxwell distribution and summed over all transitions. Even high transitions may contribute to the rates, so excitations up to H($n = 50$) need to be computed, summed over angular quantum numbers. These data would be used with velocity distributions at temperatures to $T = 10^5$ K (i.e. typical thermal energies below 1 eV).

- Other elements can be found in the stars, too. Integrated cross sections for light non-hydrogen elements (He, Ca, ...) are useful.

These topics would offer sufficient work for several master theses. In this thesis the fourth point has been chosen as a goal, whereas the fine-structure transitions in electron-hydrogen collisions and likewise the proton and other-element scattering has been postponed to the PhD thesis. Only the elastic and excitational scattering has been considered here.

As elaborated further, scattering can be roughly divided into low-energy and high-energy scattering. The former is discussed in chapter 3, together with examples of already published codes. Also an original code is presented here, which is based on exact solution of the Schödinger equation in the B-spline basis with the exterior complex scaling boundary condition. High-energy scattering is topic of chapter 4. Several Born-type approximations have been implemented and compared with experimental and other computed data.

Every one of these approaches is either mathematically valid for a certain energy range only, or the computation cost outside some energy interval increases dramatically, so that it quickly starts to be unusable with available computing facilities. Therefore, an emphasis has been put on validity limits of the methods and on the intermediate regions, where the results of different methods ought to match. Fortunately, present astrophysical models need scattering data for very low energies (around excitation thresholds) and for very high energies, which are satisfactorily described by the first and third method.

Chapter 5 contains an overview of derived scattering variables that can be extracted from the results of mentioned codes and chapter 6 discusses results of the implementations and their comparison with the experimental data.

Chapter 2

Databases

The electron-atom scattering has been an intensive research field for a long time and many data have already been produced. Several atomic databases are freely accessible on the internet, some of which also cover electron-atom scattering. Some notable representatives are:

Aladdin [4] – Contains data for elastic scattering, excitation and ionization of hydrogen for $n, n' = 1$s up to 4d. The data are from convergent close coupling (CCC) calculations by Bray [5] and match perfectly R-matrix results in low energies and Born-approximation results in high energies. The cross section curve is fitted only through several tens of points, so it represents just the scattering background and contains no resonances, see figure 2.1. Ionization cross sections were also computed by Janev and Smith [6] over finer energy mesh. Several derived rate coefficients are also stored here. Both calculations differ slightly, see fig. 2.2, without a clear clue, which results to use for a given energy range.
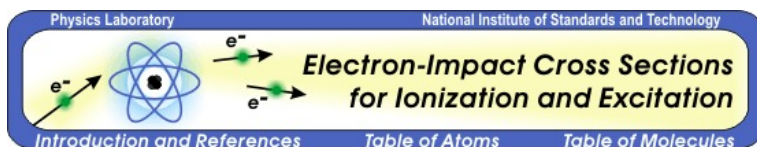
NIST Electron-impact cross sections for ionization and excitation [7] – Contains the total and differential ionization cross sections compiled from several sources and also cross sections for discrete transitions 1s→np, where $2 \leq n \leq 10$. Main resource is the report [8], data are produced by "BE-scaled" plane-wave Born approximation [9]. Comparison is done with web data [10] from a CCC calculations and with experiment [11]. Comparison between Aladdin and NIST databases for one chosen transition is presented in figure 2.3. There is also another – offline – database by NIST containing elastic data based on Dirac equation integration by Salvat *et al* [12].

原子分子数据库
Atomic & Molecular Database

CAMDB [13], Chinese atomic and molecular database – Contains no data for hydrogen reactions, just for heavier atoms.

OPEN-ADAS
Atomic Data and Analysis Structure

Open ADAS [14] – The system is meant to contain mainly spectroscopic data (spontaneous transitions etc.). Scattering data are rather scarce and for hydrogen are represented by the ionization cross section only.

2.1 Collision rates

Collisions in astrophysical applications do not occur at globally fixed energies, one needs to use thermally averaged cross sections, which describe overall effect of scattering from particles of different energies. Such quantity is called reaction rate coefficient and it can be calculated as

$$\tau(T) = \langle \sigma v \rangle_{\text{some distribution for } T} \, ,$$

typically with the Maxwell-Boltzmann velocity distribution, [15]

$$\tau(T) = \langle \sigma v \rangle_{\text{Maxw/Boltz}} = \frac{1}{\pi^{1/2}} \int_{v_{\text{th}}}^{\infty} \sigma(E_r) \frac{v_r^2}{v_T^2} e^{-v_r^2/v_T^2} \frac{\mathrm{d}v_r}{v_T} \tag{2.1}$$

with thermal velocity

$$v_T^2 = \frac{2kT}{m}$$

and threshold velocity v_{th} given as the lowest speed for which the considered transition can occur (or zero if such channel is opened for all energies). The integration variable is the relative speed between the projectile and the target atom.

It is obvious from the shape of the Maxwell-Boltzmann distribution (figure 2.4(a)) that maximal contribution to the integral comes from energies close to the thermal $E_T = mv_T^2/2 = kT$, i.e. when $v_r \approx v_T$. If the threshold velocity v_{th} (being the lower bound for v_r) is higher than the thermal velocity v_T, only the energies close to the threshold energy matter, because the distribution exponentially diminishes for relative velocities higher than thermal.

The immediate conclusion is that – generally – in the collisional excitation of cold gas only the closest neighbourhood of threshold energy affects the resulting reaction rate $\tau(T)$. This is however not a universal statement, because it may depend on the precise shape of integral cross section energy dependence. If the initial ascent of the data is comparable with the exponential decay of statistical weight in (2.1), the most influential spot may obviously be shifted.
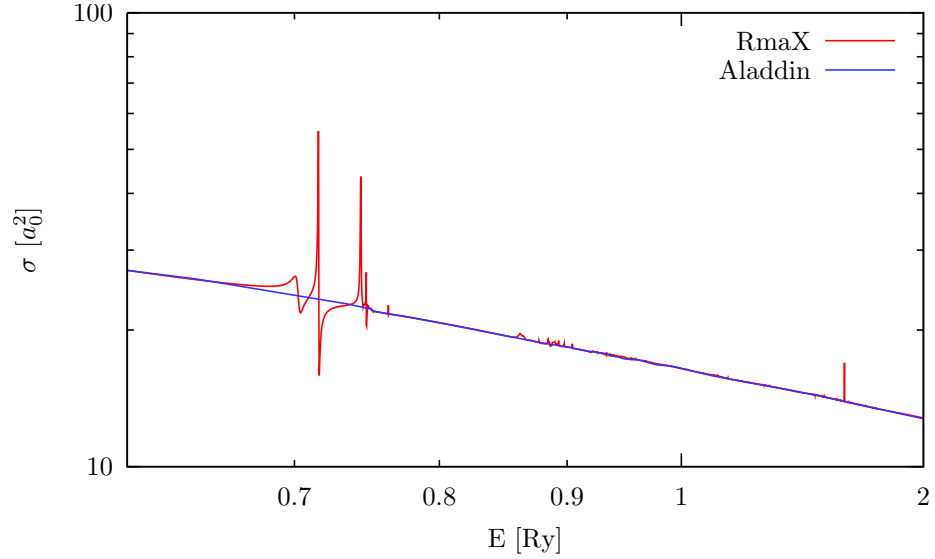
Fig. 2.1: Elastic integral cross section for e-H(1s) scattering. Aladdin data are compared to an R-matrix calculation. Apparently, all structures are missing in the database.
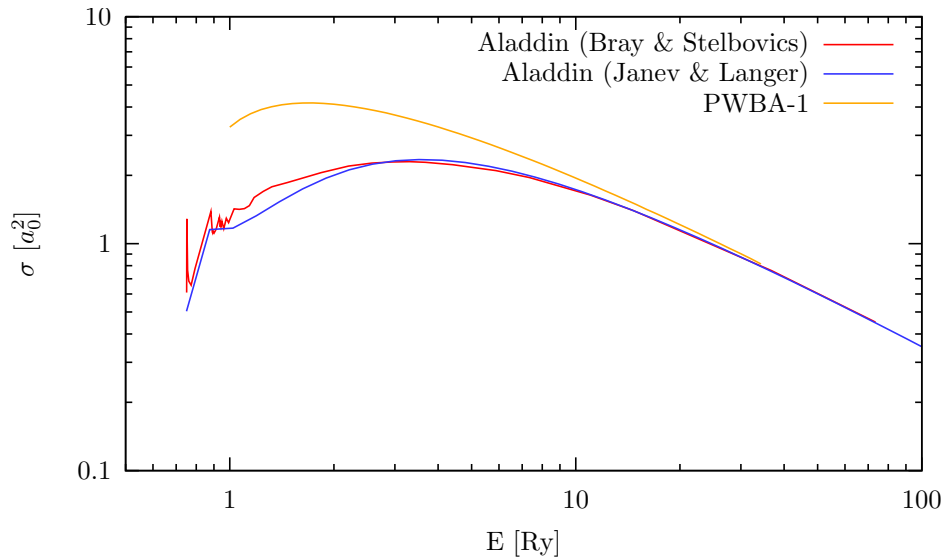
Fig. 2.2: Comparison of two datasets for an identical process, electron impact excitation H(1s) to H(2p). The Aladdin database contains both of them. Ordinary plane wave Born approximation of the first order is added for reference. Clearly, due to the discrepancy between Janev & Langer and Bray & Stelbovics datasets, the data cannot be totally relied upon approximately outside the PWBA-1 validity region. If these cross sections were used for a computation of reaction rates, one would get very distinct results, see the figure 2.4.
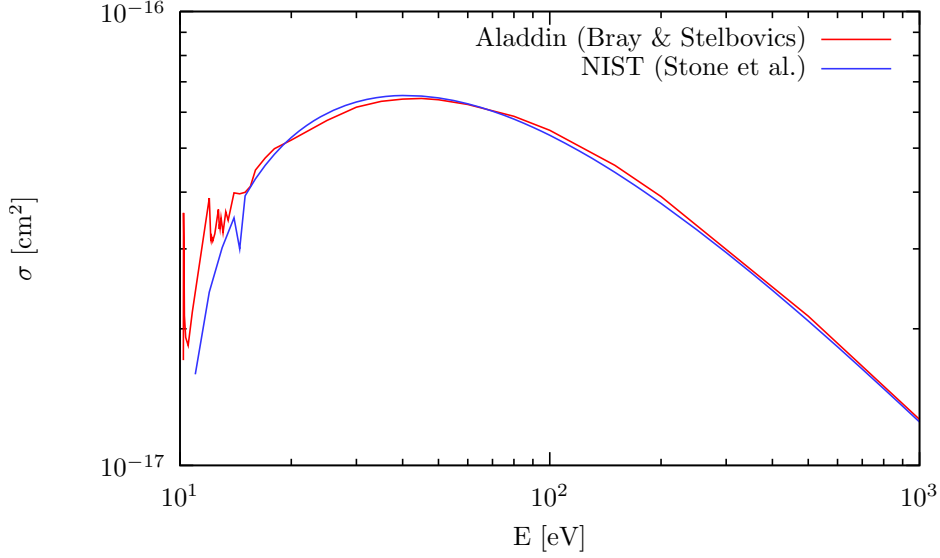
Fig. 2.3: Confrontation of Aladdin and NIST data for 1s-2p excitation of hydrogen. Both datasets satisfactorily coincide for higher energies.

(a)

(b)
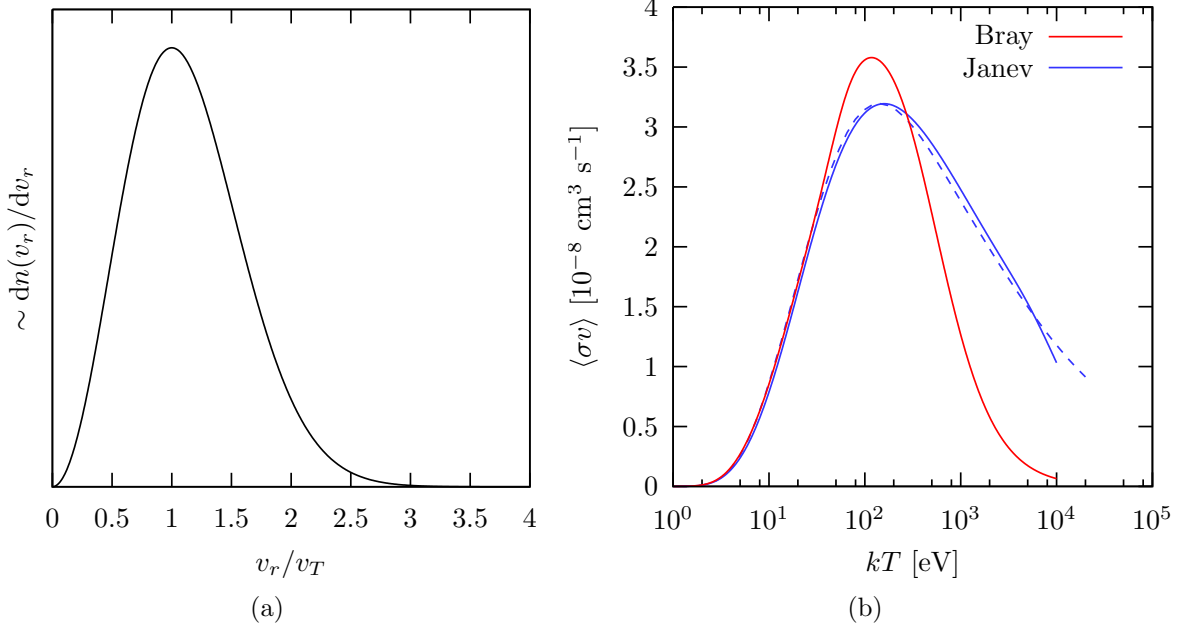
Fig. 2.4: Left graph: Maxwell-Boltzmann distribution for illustration of the necessity of accurate cross sections near transition thresholds. See the text for details. Right graph: Reaction rates computed from the slightly differing curves in 2.2. The dashed blue dependence is taken from the database as well – it is carefully integrated from a fit to the cross section data. But a straightforward trapezoidal integration (full blue curve) is apparently a good approximation. The same integration applied on results of Bray and Stelbovics (red cuve) gives a different dependence.

Chapter 3

Low energy scattering

Low energies are understood here to be the impact energy range below the ionization threshold. For hydrogen the limiting impact energy is 1 Ry or 13.6 eV. Low energy cross sections can display quite complicated behaviour in the vicinity of transition thresholds – it can contain *resonances*, both wide and narrow energy subintervals where the cross section dependence abruptly deviates from the overall trend. Resonances can be split into two general families: (a) *Feshbach resonances* and (b) *shape resonances*. Both of them arise when the projectile attaches to the atom for a short while and forms a temporary negative ion (assuming the atom was neutral prior to the collision). [16]

- Feshbach (also called *Type I* or *closed channel*) resonances lie mostly few tenths of eV below excitation thresholds and they are a manifestation of a temporary creation of a metastable double excited state. For example: when the projectile hitting the hydrogen has energy just below the H(1s)→H(2s) transition threshold, it can not excite the atom to 2s stationary state (hence the "closed channel"). Nevertheless, for a short moment it can descend in the potential well of the proton and be captured to some high stationary state. The excess energy is then used to excite the atomic electron, so that e.g. the metastable state H^-(2s4s) forms. Hydrogen negative resonances are usually designated in the following way:

$$H^-(\text{electron configuration})\,{}^S X^P \;,$$

  where S stands for total electron spin, X is the spectroscopic label (S, P, D, ...) of total angular momentum of the system and P its parity (e or o). The lowest type I resonance H^-(2s2s) ${}^1S^e$ has energy 0.702 Ry. See 3.1 for examples. The stationary atomic state which has the threshold energy is called a *parent* state. In given example, both in the text and in the figure, the parent state is the state 2s.

- Shape (also called *Type II* or *open-channel*) resonances lie always above the parent state and occur when the projectile with a specific energy is captured because of the presence of the centrifugal barrier. Naturally, S-states possess no such structures. See figure 6.7 for an example of a shape resonance.

In the next three sections the most successful methods are briefly explained, namely the *convergent close coupling*, *R-matrix theory* and finally *exterior complex scaling*. The last one has been implemented by the author and is described in greater detail together with some technicalities of the implementation.
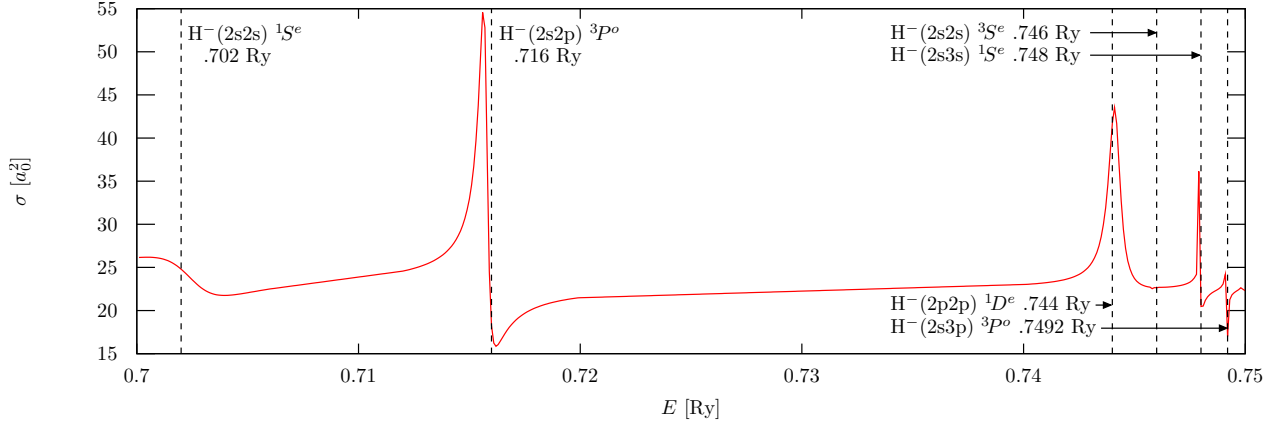
Fig. 3.1: Feshbach resonances (collected from [17], [18] and [19]) below the H(1s)→H(2s) threshold, which is at $E = 0.75$ Ry. The finite number of them is given by (a) the finite resolution of the energy grid and (b) because structures extremely close to the transition threshold will not occur due to finite radial mesh – relevant bound states would reach too far from the centre of force that they would be nonzero on the boundary. This cannot be satisfied with the ECS zero boundary condition and such resonances won't be present in the results.

3.1 Convergent close coupling method

Most relevant data in the Aladdin database have been computed using the convergent close coupling method (CCC). The usual close coupling expansion of the sought scattering wave function (for electron colliding with N-electron atom) has the form

$$\Psi_j(\mathbf{r}_1, \mathbf{r}_2, ..., \mathbf{r}_N, \mathbf{r}_0) = \mathcal{A} \sum_{i=1}^{N} \overline{\Phi}_{ij}(\mathbf{r}_1, \mathbf{r}_2, ..., \mathbf{r}_N) \frac{1}{r_0} F_i(r_0) \ . \tag{3.1}$$

The channel functions $\overline{\Phi}_i$ are obtained by coupling target states to the angular part of the projectile wave function and in such a way, that the result has a defined total angular momentum, spin, their projections to a chosen axis and parity. Substituting (3.1) into the Schrödinger equation gives rise to the set of close coupling equations for radial functions $F_j(r_0)$. The expansion (3.1) is known to converge slowly for energies near thresholds, as it does nt contain continuum states. In the *convergent* approach, the channel functions are composed of a set of n artificial basis functions, which in the limit $n \to \infty$ correctly describe the contribution of the continuum. An example of a widely used basis is

$$\xi_{k\ell}(r) = \left(\frac{\lambda_\ell (k-1)!}{(2\ell + 1 + k)!} \right)^{1/2} (\lambda_\ell r)^{\ell+1} \exp(-\lambda_\ell r/2) L_{k-1}^{2\ell+2}(\lambda_\ell r) \qquad k = 1, ..., n_\ell \ . \tag{3.2}$$

The expression (3.2) resembles hydrogen radial functions

$$P_{n\ell}(r) = r R_{n\ell}(r) = \left(\frac{\lambda(n-\ell-1)!}{2n[(n+\ell)!]^3} \right)^{1/2} (\lambda r)^{\ell+1} \exp(-\lambda r/2) L_{n-\ell-1}^{2\ell+1}(\lambda r) \ .$$

with just different normalization. The arbitrary shielding constant λ_ℓ in (3.2) stands for the scaled proton charge, $\lambda = 2Z/n$. The function L_k^α is the common generalized Laguerre polynomial.

3.2 R-matrix method

The R-matrix approach separates the physical space into two areas. One of them, the *inner region*, is mostly a sphere of some radius a that encompasses the atom and reaches far enough, so that it is possible to set short-range potentials to zero outside this sphere. The *outer* (or *asymptotic*) *region* is in non-ionizing collisions occupied only by one electron (projectile) and any exchange interactions can be ignored there. On the other hand, in the inner region the equations are solved in a non-simplified full close-coupling form. Because the region is encapsulated in a finite sphere, some operators – including the hamiltonian – would loose their hermiticity. This is avoided by rearranging the Schrödinger equation and adding a special compensating (*Bloch*) operator on both sides. [20]

$$(\hat{H}_l + \hat{\mathcal{L}} - E)\psi_l^{(\text{int})} = \hat{\mathcal{L}}\psi_l^{(\text{ext})}. \tag{3.3}$$

Solution is then sought as expansion coefficients in a given basis, ideally in the pseudostate expansion, which involves both low lying bound states as well as positive energy eigenstates simulating an effect of (free) Coulomb waves.

A "pseudostate" is a discrete state with energy higher than the ionization threshold and its function is to simulate the effect of the continuum. Carefully chosen pseudostates together with enough bound states then form an effectively complete basis set, at least for low-energy scattering. The higher the energy is, or the higher excitations we consider, the more pseudostates we need to include.

A common way how to generate a pseudostate basis is to encapsulate the system into a large but finite box and to find eigenfunctions of some hamiltonian in this box. As an example, one could compute the matrix of the hydrogen hamiltonian in some arbitrary but spacially finite basis and by diagonalization get its eigenstates.

Both inner and outer solutions are matched on the separating boundary by means of the R-matrix, which is proportional to inverse logarithmic derivative of the wave function on the boundary. The definition is

$$\psi_l(a) = R_l(E) \left[a\psi_l'(a) - B\psi_l(a) \right] ,$$

where ψ_l is the radial part of the partial wave under consideration and a is the R-matrix radius. Arbitrary dimensionless parameter B can be chosen in any way that possibly simplifies the employed numerical procedure. For a given B the Bloch operator has the form

$$\hat{\mathcal{L}}(B) = \frac{1}{2}\delta(r - a)\left(\frac{\mathrm{d}}{\mathrm{d}r} - \frac{B}{r}\right)$$

and the equation (3.3) supplemented with continuity condition $\psi_l^{\text{ext}}(a) = \psi_l^{(\text{int})}(a)$ can be solved traditionally using the Green's function mechanism. Having the solution of

$$\left(\hat{H}_l + \hat{\mathcal{L}}(B) - E\right) G_l(r, r') = \delta(r - r')$$

the R-matrix can be expressed simply as

$$R_l(E) = \frac{1}{2a}G_l(a, a) ,$$

which – expanded in some basis – is nothing else than

$$R_l(E) = \frac{1}{2a} \sum_{ij} \phi_i(a) G_{ij} \phi_j(a)^*$$

with the matrix elements G_{ij} obtainable via the inversion of

$$\left(\mathsf{G}^{-1}\right)_{ij} = \langle \phi_i | \hat{T}_l + \hat{\mathcal{L}}(B) + V - E | \phi_j \rangle. \tag{3.4}$$

The energy-independent terms of (3.4) can be diagonalized (which is the most computationally difficult task of any R-matrix package) and the inversion of the whole G^{-1} (after subtracting the remaining diagonal energy term) is then trivial.

3.3 ECS method

Both previous methods directly use the outgoing particle boundary condition in the far region, either for matching at the separating boundary (in R-matrix approach) or at the end of the grid (in the close coupling approach). Exterior complex scaling is another method serving to efficiently enforce the correct outgoing asymptotic condition. The wave function of a scattered particle oscillates and asymptotically behaves as a shifted harmonical function in the radial coordinate. If all computations are done on a special semirotated contour, cnf. fig. 3.2,
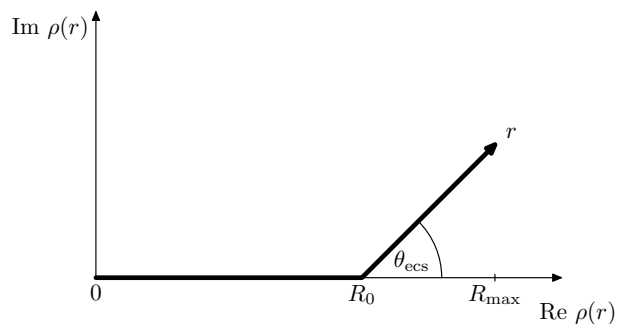
$$\rho(r) = \begin{cases} r & r \le R_0 \\ R_0 + (r - R_0)e^{i\theta_{\text{ecs}}} & r > R_0 \end{cases}$$

the imaginary part of the coordinate exponentially suppresses the harmonical function and so – at a sufficiently distant radius – a zero boundary condition can be imposed and the equations can be solved in a box without the need of considering reflections, standing waves etc. More on this is said in the "Results" chapter.

Exterior complex scaling can be used both in time-dependent and time-independent computations, though mostly ([21], [22]) the latter approach is used. In this thesis, the implementation is also time-independent.

Resulting coupled equations are solved using an expansion into a B-spline basis. B-splines are piecewise polynomial functions smooth up to the degree equal to their "order", with compact support. The other fully specifying parameter of the basis is a set of "knots", which are the starting/trailing points of distinct B-splines, see example in the figure 3.3.

Fig. 3.2: Exterior complex scaling transformation of the radial coordinate.

If the B-splines are constructed on a knot mesh at the semirotated ECS contour, they already contain derivative discontinuities stemming from sharp coordinate edge at ECS turning point. And these discontinuities are precisely transfered to approximated wave functions as appropriate, so that the turning point needs not to be treated specially (e.g. by significally

Fig. 3.3: A B-spline set with multiple knots at the beginning and at the end (which results in denser spacing of the splines in constrast with the central uniform spacing).

denser grid in its vicinity) [22], though addition of several knots *after* the turning point R_0 is actually used here to enable better approximation of incoming wave function, which has to be truncated at R_0 (and such truncation is obviously not inherent to the B-spline basis set).

3.3.1 Theory

In this section we closely follow the article of Bartlett [21].

   An unknown scattering state, which is an eigenfunction of the full system hamiltonian and from which the cross section of the studied processes can be determined, is split into two parts,

$$\Psi = \Psi_{\text{inc}} + \Psi_{\text{sc}} \ ,$$

the asymptotic "incoming particle" state Ψ_{inc} and the scattered part Ψ_{sc}, which is a solution of the driven Schrödinger equation,

$$\left(E - \hat{H} \right) \Psi_{\text{sc}} = \hat{H}_{\text{int}} \Psi_{\text{inc}} \ . \tag{3.5}$$

The state Ψ_{inc} is a product of initial atomic state and a projectile plane wave,

$$\Psi_{\text{inc}}(\mathbf{r}_1, \mathbf{r}_2) = \frac{1}{k_i r_1 r_2} P_{n_i l_i}(r_1) Y_{l_i m_i}(\hat{\mathbf{r}}_1) \cdot \sum_{lm} 4\pi \mathrm{i}^l \hat{j}_l(k_i r_2) Y_{lm}(\hat{\mathbf{k}}_i) Y_{lm}^*(\hat{\mathbf{r}}_2) \ , \tag{3.6}$$

and (anti)symmetrized with respect to electron exchange, according to the total spin,

$$\Psi_{\text{inc}}^S(\mathbf{r}_1, \mathbf{r}_2) = \frac{1}{\sqrt{2}} \left(\Psi_{\text{inc}}(\mathbf{r}_1, \mathbf{r}_2) + (-1)^S \Psi_{\text{inc}}(\mathbf{r}_2, \mathbf{r}_1) \right) \ .$$

17

(a) E = 0.7 Ry   (b) E = 4.0 Ry
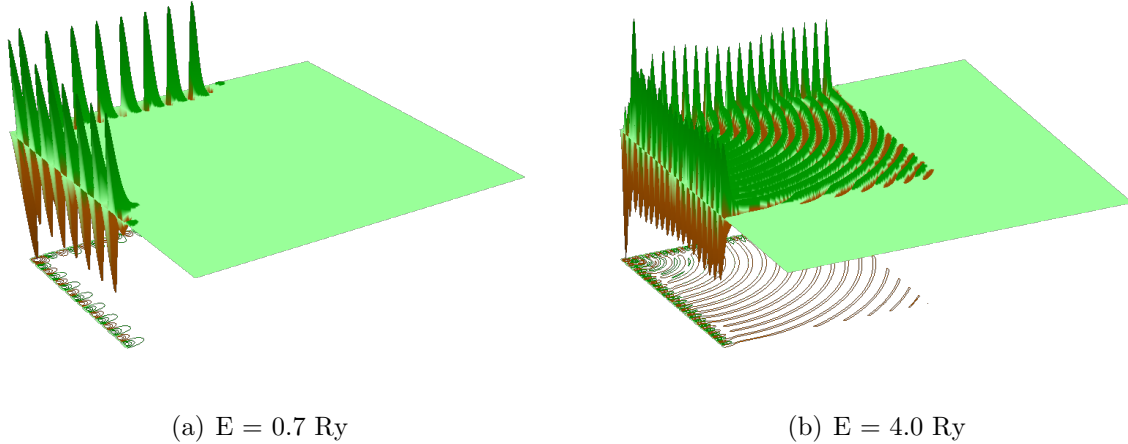
Fig. 3.4: A typical wave function $\psi_{00}^{000}(r_1, r_2)$ (defined in (3.11)), a radial part of two-particle S-partial wave, illustrating the exponential damping beyond the ECS turning point. The leftmost point of the plots is the origin of (r_1, r_2) coordinates, which continue along the edges to the right. The oscillations in the right figure indicate a nonzero contribution to ionization cross section – there is a nonzero probability of both electrons existing far from $r_1 \simeq 0$ and $r_2 \simeq 0$.

Here and in the whole text, plane waves are normalized to

$$\langle \mathbf{k} | \mathbf{k}' \rangle = (2\pi)^3 \delta^3(\mathbf{k} - \mathbf{k}') \; , \tag{3.7}$$

which saves us from carriyng the $(2\pi)^{-3/2}$ terms in every equation.

hamiltonian $\hat{H}$ is a sum of the free hamiltonian and the interaction hamiltonian,

$$\hat{H} = \hat{H}_{\text{free}} + \hat{H}_{\text{int}}$$

Free hamiltonian is the hamilton operator for electron and atom separated far away,

$$\hat{H}_{\text{free}} = -\frac{\nabla_1^2}{2} - \frac{\nabla_2^2}{2} - \frac{1}{r_1}$$

or with swapped coordinates for indirect (exchange) case, whereas the interaction hamiltonian contains the interaction between projectile and the atomic constituents, that is

$$\hat{H}_{\text{int}} = \frac{1}{r_{12}} - \frac{1}{r_2}$$

for direct case and with swapped coordinates when acting on indirect (exchange) part of incoming wave. Having the solution of equation (3.5), we can extract the scattering amplitude, which is a matrix element of $\hat{H}_{\text{int}}$ between the solution $\Psi = \Psi_{\text{sc}} + \Psi_{\text{inc}}$ and some asymptotic state Ψ_{out} that is experimentally inquired. Conventionally, Ψ_{out} is also a product of (now final) atomic state, possibly different from the original, with an outgoing plane wave of the projectile. The outgoing function should be (anti)symmetrized in similalr fashion to the incoming wave function, but since only one of these (anti)symmetrical states is measured, one can use a non-(anti)symmetrized Ψ_{out} with just a multiplicative factor of $2^{-1/2}$, which originates in the normalization of the would-be (anti)symmetrized pair.

18

For our plane wave normalization convention (i.e. without the $(2\pi)^{-3/2}$ factor) one has

$$f = -\frac{1}{2\pi} \langle \Psi_{\text{out}} | \, \hat{H}_{\text{int}} \, | \Psi \rangle \tag{3.8}$$

which can be also written as

$$f = -\frac{1}{2\pi} \langle \Psi_{\text{out}} | \, E - \hat{H}_{\text{free}} \, | \Psi_{\text{sc}} \rangle \; , \tag{3.9}$$

where the following was used: $\hat{H}_{\text{int}} = \hat{H} - \hat{H}_{\text{free}}$, $\Psi = \Psi_{\text{sc}} + \Psi_{\text{inc}}$ and $\hat{H}\Psi = E\Psi$. The multiplicative factor is a consequence of the choice (3.7). Otherwise, for traditional unit normalization, there would be $-4\pi^2$ in (3.8) and (3.9).

3.3.2 Implementation

Radial part of sought wave-functions is expanded in a B-spline basis $\{B_i\}_{i=0}^{\text{Nspline}-1}$ of a given order,

$$\Psi_{\text{sc}}^{S}(\mathbf{r}_1, \mathbf{r}_2) = \sum_{LM} \Psi_{\text{sc}}^{LMS}(\mathbf{r}_1, \mathbf{r}_2) \; , \tag{3.10}$$

$$\Psi_{\text{sc}}^{LMS}(\mathbf{r}_1, \mathbf{r}_2) = \sum_{l_1 l_2} \psi_{l_1 l_2}^{LMS}(r_1, r_2) \mathcal{Y}_{l_1 l_2}^{LM}(\hat{\mathbf{r}}_1, \hat{\mathbf{r}}_2) \; , \tag{3.11}$$

$$\psi_{l_1 l_2}^{LMS}(r_1, r_2) = \frac{1}{r_1 r_2} \sum_{ij} \psi_{l_1 l_2, ij}^{LMS} B_i(r_1) B_j(r_2) \; , \tag{3.12}$$

and when projecting the equation (3.5) on a bipolar spherical function $\langle \mathcal{Y}_{l_1 l_2}^{LM} |$ to get rid of angular dependence, and on a pair of B-splines to get rid of any coordinate dependence at all and keep only matrix elements, one arrives at a matrix equation for components of $\psi_{l_1 l_2}^{LMS}(r_1, r_2)$,

$$\left[\left(E S_{ik} S_{jl} - H_{ijkl}^{(1)} - H_{ijkl}^{(2)} \right) \delta_{l_1}^{l_1'} \delta_{l_2}^{l_2'} - \sum_{\lambda} f_{l_1 l_2 l_1' l_2'; L}^{\lambda} R_{ijkl}^{\lambda} \right] \psi_{l_1' l_2', kl}^{LMS} = \chi_{l_1 l_2, kl}^{LMS}$$

with

$$H_{ijkl}^{(1)} = \frac{1}{2} D_{ik} S_{jl} + \frac{1}{2} l_1 (l_1 + 1) M_{ik}^{(-2)} S_{jl} - M_{ik}^{(-1)} S_{jl} \; ,$$

$$H_{ijkl}^{(2)} = \frac{1}{2} S_{ik} D_{jl} + \frac{1}{2} l_2 (l_2 + 1) S_{ik} M_{jl}^{(-2)} - S_{ik} M_{jl}^{(-1)}$$

or symbolically

$$\left[\mathsf{Id}_1 \otimes \mathsf{Id}_2 \otimes \left(E\mathsf{S} \otimes \mathsf{S} - \mathsf{H}^{(1)} - \mathsf{H}^{(2)} \right) + \sum_{\lambda} \mathsf{f}_L^{\lambda} \otimes \mathsf{R}^{\lambda} \right] \psi^{LMS} = \chi^{LMS} \; ,$$

$$\mathsf{H}^{(1)} = \frac{1}{2} \mathsf{D} \otimes \mathsf{S} + \frac{1}{2} l_1 (l_1 + 1) \mathsf{M}^{(-2)} \otimes \mathsf{S} - \mathsf{M}^{(-1)} \otimes \mathsf{S}$$

$$\mathsf{H}^{(2)} = \frac{1}{2} \mathsf{S} \otimes \mathsf{D} + \frac{1}{2} l_2 (l_2 + 1) \mathsf{S} \otimes \mathsf{M}^{(-2)} - \mathsf{S} \otimes \mathsf{M}^{(-1)} \; .$$

Symbol $\otimes$ stands for Kronecker product ("flattened tensor product") and matrices have following meanings:

- Matrix Id_1 is identity of rank equal to maximal allowed angular momentum l_1. Analogically for Id_2 .

- Matrix D is the matrix of derivative overlaps of B-splines. It can be shown for B-splines basis which is zero at boundaries that in such case

$$\langle B_i| \left(-\frac{\mathrm{d}2}{\mathrm{d}x^2}\right) |B_k\rangle = +\int_a^b \frac{\mathrm{d}B_i}{\mathrm{d}x}\frac{\mathrm{d}B_k}{\mathrm{d}x} \equiv +D_{ik} \ .$$

- Matrix S is just the standard overlap matrix of the B-spline basis,

$$S_{ik} = \langle B_i| B_k\rangle \ .$$

- Matrix $\mathsf{M}^{(\alpha)}$ is matrix element of power of coordinate (also called "integral moment" in the source code),

$$M_{ik}^{(\alpha)} = \langle B_i(r)| \, r^\alpha \, |B_k(r)\rangle \ .$$

- Matrix R^λ is matrix of four-B-spline multipole integrals for multipole λ,

$$R_{ijkl}^\lambda = \int_a^b \int_a^b B_i(r_1)B_j(r_2)\frac{r_<^\lambda}{r_>^{\lambda+1}}B_k(r_1)B_l(r_2)dr_1 dr_2 \ ,$$

flattened so that i and j form one multi-index $[ij]$ and the other indices the multi-index $[kl]$.

- Matrix f_L^λ is the angular part of the reduced matrix element,

$$\langle l_1 l_2||\frac{1}{r_{12}}||l_1' l_2'\rangle_L = \sum_\lambda f_{l_1 l_2 l_1' l_2';L}^\lambda \frac{r_<^\lambda}{r_>^{\lambda+1}} \ ,$$

flattened so that l_1 and l_2 form one multi-index $[l_1 l_2]$ and the other two indices the second. The symbol $f_{l_1 l_2 l_1' l_2';L}^\lambda$ stands for a product of Wigner 3j- and 6j- coupling coefficients, see [21].

Finally, the symbol χ^{LMS} stands for the projection of the right hand side, which is

$$\chi_{l_1 l_2,ij}^{LMS} = \frac{1}{k_f}\sum_\ell \mathrm{i}^\ell \sqrt{2\pi(2\ell+1)}C_{l_i m_i \ell 0}^{LM} \left\{\chi_{l_1 l_2,ij}^{LMS,(1)} + (-1)^{S+\Pi}\chi_{l_1 l_2,ij}^{LMS,(2)}\right\} \tag{3.13}$$

with

$$\chi_{l_1 l_2,ij}^{LMS,(1)} = \left(\sum_\lambda f_{l_1 l_2 l_i \ell;L}^\lambda R_{ijkl}^\lambda - \delta_{l_1}^{l_i}\delta_{l_2}^\ell S_{ik}M_{jl}^{(-1)}\right)\left[P_{n_i l_i}(r_1)\right]_k \left[\hat{j}_\ell(k_i r_2)\right]_l$$

$$\chi_{l_1 l_2,ij}^{LMS,(2)} = \left(\sum_\lambda f_{l_1 l_2 \ell l_i;L}^\lambda R_{ijkl}^\lambda - \delta_{l_1}^\ell \delta_{l_2}^{l_i} M_{ik}^{(-1)}S_{jl}\right)\left[\hat{j}_\ell(k_i r_1)\right]_k \left[P_{n_i l_i}(r_2)\right]_l$$

or symbolically

$$\chi^{LMS} = \frac{1}{k_f}\sum_\ell \mathrm{i}^\ell \sqrt{2\pi(2\ell+1)}C_{l_i m_i \ell 0}^{LM} \left\{\chi^{LMS,(1)} + (-1)^{S+\Pi}\chi^{LMS,(2)}\right\} \tag{3.14}$$

with

$$\chi^{LMS,(1)} = \left(\sum_\lambda \mathsf{f}_L^\lambda \otimes \mathsf{R}^\lambda - \mathsf{Id}_1 \otimes \mathsf{Id}_2 \otimes \mathsf{S} \otimes \mathsf{M}^{(-1)} \right) \cdot \Delta^{l_i} \otimes \Delta^\ell \otimes \mathsf{P}_{n_i l_i} \otimes \mathsf{j}_{\ell, k_i} \ ,$$

$$\chi^{LMS,(2)} = \left(\sum_\lambda \mathsf{f}_L^\lambda \otimes \mathsf{R}^\lambda - \mathsf{Id}_1 \otimes \mathsf{Id}_2 \otimes \mathsf{M}^{(-1)} \otimes \mathsf{S} \right) \cdot \Delta^\ell \otimes \Delta^{l_i} \otimes \mathsf{j}_{\ell, k_i} \otimes \mathsf{P}_{n_i l_i} \ .$$

Here, the one-dimensional vectors Δ^ℓ are zero vectors with only one element equal to one at position ℓ. P- and j- vectors are components of respective function (hydrogen radial function multiplied by radius or Riccati-Bessel function) in chosen B-spline basis. These expansions are determined from the solution of the matrix equations

$$(\mathsf{S})_{ij} \left(\mathsf{P}_{n_i l_i} \right)_j = \int_0^{R_{\max}} B_i(r) P_{n_i l_i}(r) dr \ ,$$

$$(\mathsf{S})_{ij} \left(\mathsf{j}_{l, k_i} \right)_j = \int_0^{R_{\max}} B_i(r) \hat{j}_l(k_i r) dr \ .$$

Factor $C_{l_i m_i \ell 0}^{LM}$ in the expressions (3.13), (3.14) is a Clebsch-Gordan coefficient and the zero projection of ℓ-momentum reflects the deliberate choice of scattering axis along the projectile momentum, so that its angular momentum projection is zero.

3.3.3 Restrictions on potential

Exterior complex scaling of the right hand side poses a serious problem for typical (not exponentially decreasing) potentials. One of the factors in the right hand side is the Riccati-Bessel function $\hat{j}$, which exponentially diverges under ECS transformation. To avoid this, potential $\hat{H}_{\mathrm{int}}$ is artificially truncated at (or before) the turning point R_0, which has several consequences for the numerical construction:

- In equations (3.8)-(3.9), the radial integration is done only up to $r_1, r_2 = R_0$ and not further.

- Matrices $\mathsf{M}^{(-1)}$ and R^λ in (3.13), (3.14) are to be computed, again, for $r_1, r_2 \leq R_0$. These are referenced as "truncated overlap matrices" in the source code.

To preserve the physical sense of the equation, the enforced truncation is also done in the left hand side – in the hamiltonian –, in simillar manner. The truncation is not done by a step function $\theta(|r| - R)$ but using a smooth rapidly decreasing distribution

$$\zeta(r) = \begin{cases} \tanh\left(\alpha(R - r)\right) & (\mathrm{Im}\, r = 0) \\ 0 & (\mathrm{Im}\, r > R) \end{cases} \ .$$

Sharp truncation might result in reflections at the potential step, which would affect the results. The parameter α controls the slope of the decreasing region.

21

3.3.4 Cross section

As was said above, the scattering amplitude is

$$f = -\frac{1}{2\pi} \langle \Psi_{\text{out}}| E - \hat{H}_{\text{free}} |\Psi_{\text{sc}}\rangle_{R_0} \ ,$$

where the subscript R_0 means that the radial integration is done only for radii less than R_0, because the original matrix $\hat{H}_{\text{int}}$ has to be truncated at such distance to avoid far-region divergence. The outgoing – detected – wavefunction Ψ_{out} has a form simillar to (3.6), with re-placed initial to final quantum numbers. Substituting such expansion into the equation (3.8) and once again using zero boundary condition of the chosen B-spline basis when doing per parts integration one easily arrives at the formula for cross section

$$\sigma^S = \frac{2}{k_i k_f} \sum_{\ell L L' ab} C_{l_f m_f \ell 0}^{L m_f} C_{l_f m_f \ell 0}^{L' m_f} \left| \psi_{l_f \ell, ab}^{L m_f S} W[P]_a S[j]_b + \psi_{l_f \ell, ab}^{L' m_f S} S[P]_a W[j]_b \right|^2 \ ,$$

where $W[P]_i$ and $W[j]_i$ stand for wronskian (evaluated at $R_0 - \varepsilon$) of the i-th B-spline and the (final) hydrogenic or Riccati-Bessel function, and $S[P]_i$ and $S[j]_i$ stand for the (truncated) overlap integrals of the i-th B-spline and the (final) hydrogenic or Riccatti-Bessel function. In the limit of $R_0 \to \infty$ the array $W[P]$ will contain only zeros (P is an exponentially decreasing function), so the whole term can be neglected.

Total spin-weighted cross-section is

$$\sigma_{\text{tot}} = \sum_S \frac{2S + 1}{4} \sigma^S \ .$$

3.3.5 Implementation details

Most of the matrices are sparse. Matrices of integral moments are symmetrical and have exactly `2*order+1` diagonals. Matrices constructed from them by means of the Kronecker product have diagonal count equal to the second power of previous number etc. The rank of these matrices, proportional to B-spline count, is typically two orders higher, which leaves only units per cent elements non-zero. Matrices are stored in the compressed row storage format or coordinate ("ijv") format and the program uses several external libraries for heavy algebraical tasks, namely linear system solution and conversions between storage formats. Solution of all matrix equations is implemented as a refined LU-decomposition as offered by two high-performance libraries.

- Intel MKL Direct Sparse Solver – Wrapper of the commercial Pardiso solver, "a thread-safe, high-performance, robust, memory efficient and easy to use software for solving large sparse symmetric and unsymmetric linear systems of equations on shared-memory and distributed-memory multiprocessors" [23]. This solver has even so called "out of core" capabilities, which enable it to run on system with low memory. Large auxiliary disk files are then used.

- UMFPACK – Free (under GNU GPL terms) library for solving unsymmetric sparse linear systems, using the Unsymmetric MultiFrontal method [24]. This package can be used on systems without Intel MKL and when used together with optimized OpenBLAS it doesn't do any worse than Pardiso.

Every partial wave Ψ^{LMS} is expanded in terms of "coupled angular-momentum states" ψ_{l_1,l_2}^{LM}. In theory, the angular momentum quantum numbers should run over all non-negative integers and couple together the Schrödinger equations for each of pairs (l_1, l_2). Thus, the matrix of the equation set gains a block structure with off-diagonal blocks represented by elements of $\mathsf{f} \otimes \mathsf{R}$ and diagonal blocks represented by the kinetic energy and the potential in the proton Coulomb field. In reality, the numbers l_1 and l_2 are obviously limited, typically to one-digit numbers. Still, the matrix $E - \mathsf{H}$ can easily reach huge ranks of order up to several milions. Direct LU-factorization of such a matrix is unthinkable with presently available computer memories. Purely iterative methods are unusable as well; the convergence of iteratively refined solution for so large matrices is extremely slow, many iterations are needed, which gives rise to numerical rounding errors.

In the end, a hybrid method has been used, where individual diagonal blocks are LU-factorized and used as a block preconditioner of Jacobi type for a preconditioned conjugate gradients algorithm. With this approach the LU-factorizations do not consume such a vast amount of memory and a machine with several tens of GiB-s of memory suffices to produce converged results.

Compute $r^{(0)} = b - Ax^{(0)}$ for some initial guess $x^{(0)}$
for $i = 1, 2, ...$
    solve $M \cdot z^{(i-1)} = r^{(i-1)}$
    $\rho_{i-1} = r^{(i-1)} \cdot z^{(i-1)}$
    if $i = 1$
        $p^{(1)} = z^{(0)}$
    else
        $\beta_{i-1} = \rho_{i-1}/\rho_{i-2}$
        $p^{(i)} = z^{(i-1)} + \beta_{i-1} p^{(i-1)}$
    endif
    $q^{(i)} = A \cdot p^{(i)}$
    $\alpha_i = \rho_{i-1}/\left(p^{(i)} \cdot q^{(i)}\right)$
    $x^{(i)} = x^{(i-1)} + \alpha_i p^{(i)}$
    $r^{(i)} = r^{(i-1)} - \alpha_i q^{(i)}$
   check convergence; continue if necessary
end

Fig. 3.5: Preconditioned conjugate gradients for solution of the system $A \cdot x = b$ [25]. The matrix M is an arbitrary preconditioner, in present implementation a block-diagonal of A, the main matrix of the system. Dot symbol stands for scalar product of the operands.

3.4 Programs

The collisional cross sections use to be computed using the close-coupling expansion, which is a method that treats all the electrons (both atomic and projectile) as indistinguishable and performs full antisymmetrization. Most large and successful computation packages use the
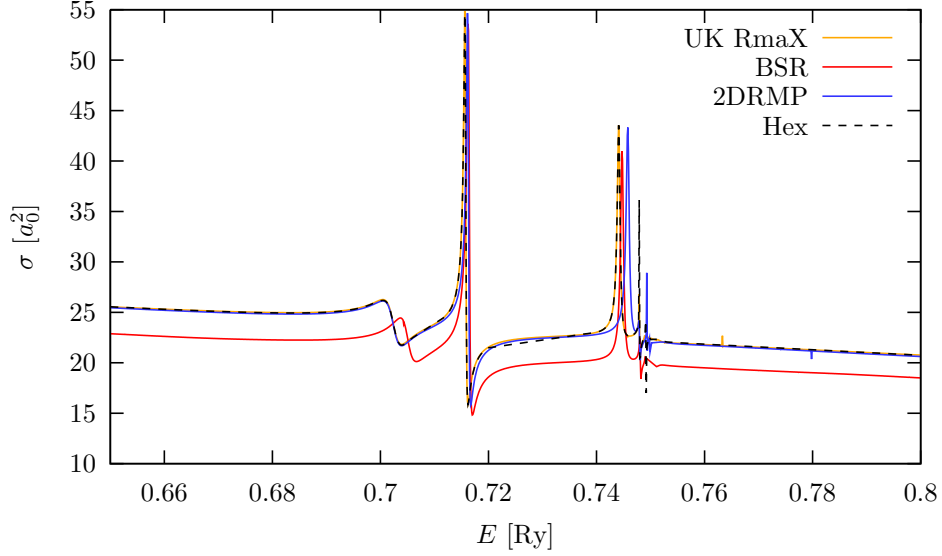
Fig. 3.6: Confrontation of mentioned R-matrix packages for basic H(1s)→H(1s) elastic scattering. Though all of them have been computed for a sufficient (convergent) number of partial waves, still there are some discrepancies. If the RmaX results are taken as reference, the BSR results appear shifted down, whereas 2DRMP seems to misplace some resonances, most notably the H$^-$(2p2p) $^1D^e$. Results of RmaX have been more or less verified by our program Hex.
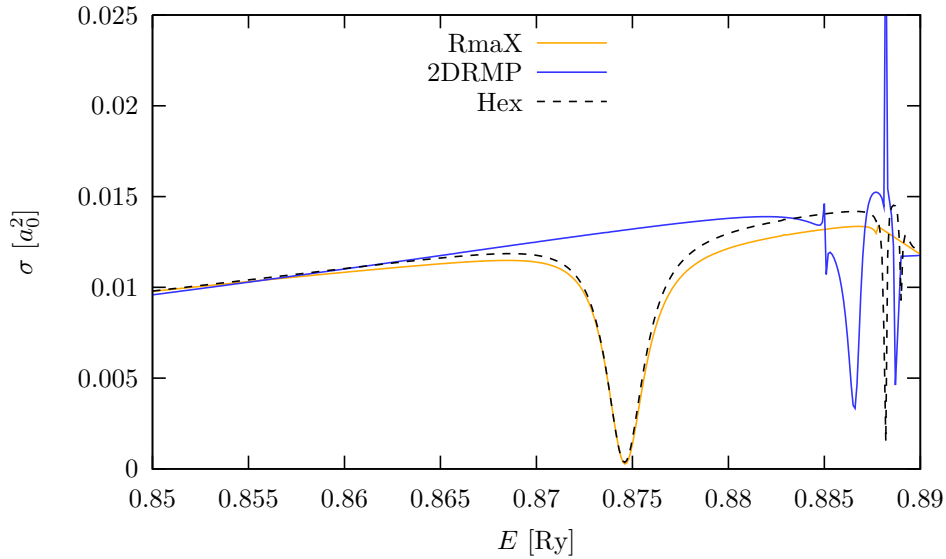
Fig. 3.7: Comparison of $^1P^o$ partial wave cross section for H(1s)→H(1s) elastic scattering. Again, RmaX and Hex give very similar results. On the contrary 2DRMP gives the "dip" resonance shifted by ~ 0.013 Ry. The results of BSR did not fit into the figure at all, they were about ten times larger than the rest.

R-matrix method and certainly the three presented here do so. Still, their results differ, as can be seen for example of the figure 3.6 or below. Comparison is done also with the original code Hex.

3.4.1 BSR

BSR by Zatsarinny [26] is a package that uses a B-spline basis to expand the sought wave functions. The same set of B-splines thus serves as a basis of the R-matrix. It offers a lot of flexibility as it allows usage of non-orthogonal target orbitals, which may contribute to better target description even with a few orbitals. Unfortunately, for a reasonable description of excitation one would need to include pseudostates, which are (in the hydrogen case) impossible to generate using supplied atomic sctructure tools. As BSR lacks the possibility to include pseudostates, only elastic scattering results for low energies are trustworthy. As pointed out by Callaway in [27], pseudostates are necessary for the correct description even of 1s $\rightarrow$ 2s excitation. Moreover, the radial grid in BSR is hardcoded in logarithmic way, which is appropriate for true bound state but not for discretized continuum states, that can vary rapidly (oscillate) even for distant radii.

3.4.2 2DRMP

2DRMP by the Belfast group [28] uses IERM method – intermediate energy R-matrix –, which differs from the previous RMPS – R-matrix with pseudo-states – by including true two-particle continuum basis wave functions in the expansion of the wave function of the whole system, not the artificial pseudo-orbitals. This method is not as extensible as the RMPS (concerning the number of electrons) and is easily implemented just for 1+1 electron systems. On the other hand, as it allows to treat both electrons identically – even if both are in contiuum – it can very efficiently describe ionization processes. The name 2DRMP reflects this idea of two independent and equally described radial coordinates.

While the R-matrix radius in the traditional R-matrix divides the r coordinate into two semi-lines, the 2D R-matrix approach divides the $(r_1 > 0, r_2 > 0)$ quadrant into two 2D regions. Folowing the precise R-matrix scheme is computationally costly here, so the inner 2D region is divided into "sectors" and each of these sectors is solved independently. This allows parallelization of some stages of the computation. Recently, the relevant part was implemented on GPU [29].

Though for some energies the results are quite good, like in fig. 3.6, there are areas where 2DRMP fails, too; see figs. 3.7 and 3.8.

3.4.3 UK RmaX

UK RmaX by the University of Strathclyde group [30] is a follower and extension of RMA-TRX1 [31], the first large low-energy scattering computation system. It uses the pseudostate expansion, which is easy to generate for hydrogen as well using appended atomic structure package (called autostructure), and is available in a parallelized version, which allows the user to speed up the computation when using a multiprocessor system. It, too, has some drawbacks, which are illustrated in the "Results" chapter in figures 6.6 and 6.7.

25

As all listed programs use the same method based on R-matrix matching at the separating boundary between the close-coupling (antisymmetrized) and asymptotic (non-antisymmetrized) region. A slightly different one was implemented by the author of this thesis to allow a comparison across different methods and to support the results of one of the above mentioned packages.
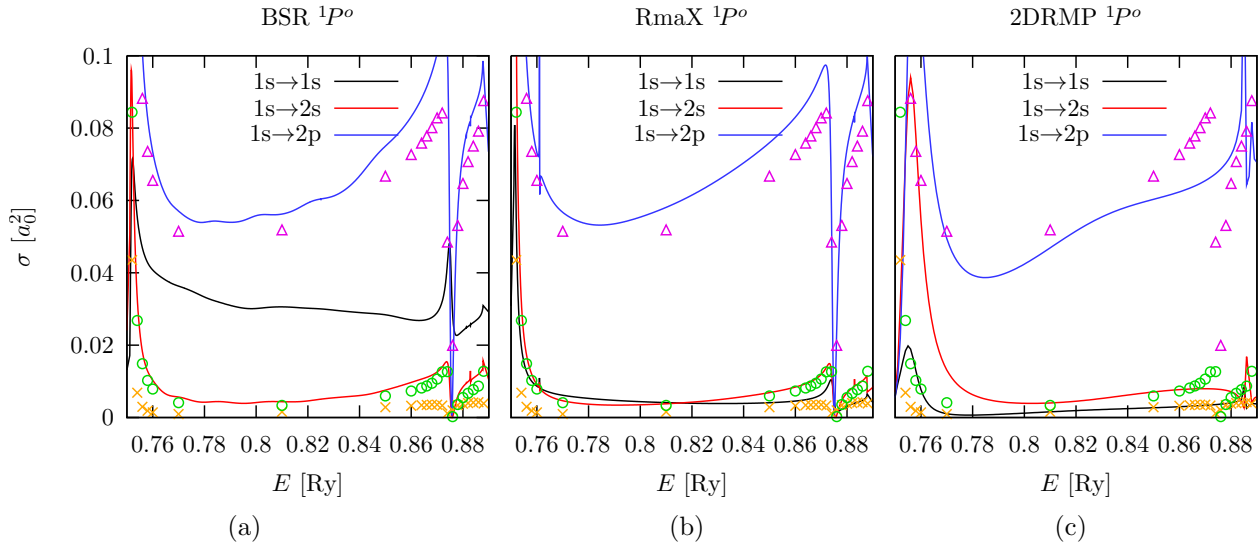
Fig. 3.8: The three low-energy R-matrix packages compared with benchmark data of Bartschat *et al* [32]. The elastic cross section of BSR (black curve) is by a factor off the data.

Chapter 4

High energy scattering

When dealing with the scattering at energies larger than several times the ionization threshold one has to keep in mind that accurate approximation of wave function requires significantly finer radial mesh division or finite element basis functions to simulate rapid oscillations than in the low energy scattering.

All low energy methods eventually arrive at a limit, when they stop to be efficient and computationally bearable. High energies are thus a domain of perturbation aproaches, which consider rather the effective potentials than detailed inter-electron interactions. In [2] several published programs were presented, namely Elastic [33] and Elsepa [12]. As their name suggests, they work only in the elastic regime; that is also a necessary consequence of the static-potential method. Event hough the results of these programs in elastic scattering are quite good, for general usage they are inadequate, because the excitation crosss sections are needed as well.

Excitations had been computed by the means of eikonal approximation or the (distorted wave) Born approximation, to be described below, and there actually exist some their implementations, Eikonal [34] and DWBA (appended to [35]). However, both are limited to transitions from the ground state and DWBA fails for energies above ~ 30 Ry and Eikonal can be used just for several fixed final states. For these reasons, alternative universal methods have been investigated, as described in the following sections.

4.1 PWBA and BE scaling

The most famous asymptotic approximation is the so called "(plane wave) Born approximation". It is a simplification of the Lippman-Schwinger equation

$$\Psi^{(+)} = \Psi_{\text{inc}} + \hat{G}^{(+)}\hat{H}_{\text{int}}\Psi^{(+)}$$

by recurrent substitution and deliberate truncation of the series,

$$\Psi^{(+)} \approx \Psi_{\text{inc}} + \hat{G}^{(+)}\hat{H}_{\text{int}}\Psi_{\text{inc}} + \hat{G}^{(+)}\hat{H}_{\text{int}}\hat{G}^{(+)}\hat{H}_{\text{int}}\Psi_{\text{inc}} + ... \ .$$

The T-matrix in the first Born approximation then simply reads

$$T = \langle \Psi_{\text{out}} | \hat{H}_{\text{int}} | \Psi_{\text{inc}} \rangle \ , \tag{4.1}$$

where the left or right vector may be (anti)symmetrized to compute simultaneously direct and indirect scattering amplitude.

This naive and straightforward method was solved in [2] and gives correct results for energies higher than approximately 1 MeV. Higher-order Born approximation would involve computation of many-dimensional integrals containing Green's functions. A feasible alternative is a certain modification of states under consideration, which is presented in the next section.

However, if only cross sections are needed, a simple yet powerful scaling method was discovered [9], which transforms first-order plane wave cross sections so that they very well match the experimental data and other more sophisticated theories as well. The method is called BE-scaling and modifies the general formula for cross section

$$\sigma(E_i) = \frac{4\pi a_0 R}{E_i} \tilde{\Omega}(E_i) \ ,$$

into

$$\sigma_{\mathrm{BE}}(E_i) = \frac{4\pi a_0 R}{E_i + B + E} \tilde{\Omega}(E_i) \ ,$$

i.e. applies the transformation

$$\sigma_{\mathrm{BE}}(E_i) = \sigma(E_i) \frac{E_i}{E_i + B + E} \ .$$

Here, E_i is the kinetic energy of the incident projectile, R Rydberg energy, B ionization energy ("binding energy" of the initial state) and E excitation energy of the final state with respect to the initial state. The quantity $\tilde{\Omega}$, is proportional to the collision strength (5.3).

BE-scaling works best for the dipole-allowed transitions, e.g. 1s→2p, but is less satisfactory for dipole-forbidden transitions, e.g. 1s→2s. The reason is, that plane wave Born approximation of the second order cannot consider multistep transitions like 1s→2p→2s, which would occur more frequently than the direct process 1s→2s. Resulting cross section is thus smaller than in reality. Some examples are in the figures 4.1 and 4.2. Theoretical justification of BE-scaling is yet to be discovered; at present it serves as a mere empiric rule.

4.2 DWBA method

There exists an extension of the plane wave Born approximation called the *distorted wave Born approximation*. Plane waves are substituted by *distorted waves*, which solve the following equation:

$$\left(-\frac{\nabla^2}{2} + U_i - \frac{k_i^2}{2}\right)\chi_i^{(+)} = 0 \ , \tag{4.2}$$

where U_i is an arbitrary *distorting potential*. Whenever $U_i \equiv 0$, the solutions $\chi_i^{(+)}$ are just ordinary plane waves. The scattering amplitude cannot be then evaluated simply from (4.1). The correct expression for T-matrix is the *two-potential formula* [35] [36]

$$T = (N+1)\left\langle \chi_f^{(-)}\psi_f \left| V - U_f \right| \mathcal{A}\Psi_i^{(+)}\right\rangle + \left\langle \chi_f^{(-)}\psi_f \left| U_f \left| \psi_i \beta_i\right\rangle \right. \ , \tag{4.3}$$

where:

- V is the full potential felt by projectile. In the case of hydrogen

$$V(\mathbf{r}_1, \mathbf{r}_2) = -\frac{1}{|\mathbf{r}_2|} + \frac{1}{|\mathbf{r}_1 - \mathbf{r}_2|} \;.$$

  The potential has this form only when acting on wave function describing the direct scattering (electron no. "1" is the atomic electron). When acting on the exchange term, the coordinates would be swapped.

- U_f is the final distorting potential that defines states χ_f through the equation (4.2). The potential can be truly arbitrary; nevertheless, a common choice is a sphericaly symmetrical potential of the electron cloud in final (or initial) state,

$$U_f(r_2) = \frac{1}{4\pi} \int \langle \psi_f(\mathbf{r}_1) | V(\mathbf{r}_1, \mathbf{r}_2) | \psi_f(\mathbf{r}_1) \rangle \mathrm{d}\Omega_2 \;.$$

- $\Psi_i^{(+)}$ is the full solution of the (N+1)-particle Schrödinger equation or, equivalently, of the Lippman-Schwinger equation

$$\Psi_i^{(+)} = \psi_i \chi_i^{(+)} + \hat{G}^{(+)}(V - U_i)\psi_i \chi_i^{(+)}, \qquad \hat{G}^{(+)} = (E - \hat{H} - \mathrm{i}\eta)^{-1} \tag{4.4}$$

  As it is apparent, this solution is not automatically antisymmetrical with respect to the particle exchange. The operator $(N+1)\mathcal{A}$ takes care of the manual antisymmetrization.

- $\chi_f^{(-)}$ is a distorted wave (by the distorting potential U_f) satisfying incoming wave asymptotic condition. It holds that one can get $\chi_f^{(-)}$ from $\chi_f^{(+)}$ by complex conjugation of the radial part. [35]

- ψ_i and ψ_f are the initial and final atomic states.

- β_i is the initial plane wave.

The first Born approximation, which contains no Green's function, is done by taking only the first term in (4.4). This leads to

$$T \approx T_1 = (N+1)\left\langle \chi_f^{(-)}\psi_f \middle| V - U_f \middle| \mathcal{A}\psi_i \chi_i^{(+)} \right\rangle + \left\langle \chi_f^{(-)}\psi_f \middle| U_f \middle| \psi_i \beta \right\rangle \tag{4.5}$$

which for hydrogen means $T_1 = T_{\text{direct}} + (-1)^S T_{\text{exchange}}$, where

$$T_{\text{direct}} = \left\langle \chi_f^{(-)}\psi_f \middle| V \middle| \psi_i \chi_i^{(+)} \right\rangle + \left\langle \chi_f^{(-)} \middle| U_f \middle| \beta_i - \chi_i^{(+)} \right\rangle \delta_{fi}$$

$$T_{\text{exchange}} = \left\langle \chi_f^{(-)}\psi_f \middle| V' \middle| \chi_i^{(+)}\psi_i \right\rangle - \left\langle \chi_f^{(-)} \middle| U_f \middle| \psi_i \right\rangle \left\langle \psi_f \middle| \chi_i^{(+)} \right\rangle$$

The U_i, U_f depend only on the projectile coordinate. The V' contains swapped coordinates as mentiones above, so that it is integrated with the projectile coordinates.

The computation has been done in the following way: The equation (4.2) is solved numerically for every partial wave (χ_ℓ) using a routine from the O$_2$scl library [37]. We have a boundary condition to satisfy, which has the standard scattering form

$$\chi_\ell(k, r) \propto \mathrm{e}^{\mathrm{i}\delta_\ell} \sin\left(kr - \frac{\pi\ell}{2} + \delta_\ell\right) \;. \tag{4.6}$$

Unfortunately, such a form is not really helpful, as we do not know the phase shift δ_ℓ. The solution χ_ℓ ought to be regular, so we principally could start from a zero initial condition in $r = 0$. In that case, however, a common initial value solver will return a trivial (zero) solution, which certainly solves (4.2). Assuming that the repulsive centrifugal barrier is much more influential around the origin than the distorting potential $U(r)$, which behaves as r^{-1}, whereas the barrier behaves as r^{-2}, the $U(r)$ can be neglected for $r \approx 0$ and we are left with a standard spherical Riccati-Bessel equation. Thus, we can use nonzero initial value condition *near* the origin as if we were computing regular Riccati-Bessel function and start onward. Asymptotics of Riccati-Bessel function near zero is

$$\hat{j}_\ell \propto \frac{2^\ell \ell!}{(2\ell + 1)!} x^{\ell+1}, \qquad \hat{j}'_\ell \propto \frac{2^\ell (\ell + 1)!}{(2\ell + 1)!} x^\ell , \tag{4.7}$$

so if we use the initial conditions in the form

$$\chi_\ell(k, \delta) \simeq \varepsilon_1 \qquad \text{and} \qquad \frac{d\chi_\ell}{dr}(k, \delta) = \varepsilon_2$$

with δ being the grid discretization and ε_i being arbitrary small numbers differing by the same factor as the asymptotic expansion of the regular Riccati-Bessel function, that is with the ratio

$$\frac{\varepsilon_1}{\varepsilon_2} = \frac{\delta}{\ell + 1} ,$$

we ought to get correct behaviour. For the solution a callback library function is used, which executes several steps at once to advance solution from the point r_1 to a near point r_2. After every such step we normalize the solution, if necessary, to avoid overflow, which is otherwise inevitable when using considerably larger initial conditions than the correct ones in (4.7). It would be easiest to use (4.7) directly when specifying the initial conditions; however, for high partial waves ($\ell > 80$) the formulas – evaluated in common double precition – would underflow to zero and the solution would collapse (we would get the trivial solution again). For this reason (and because of possible roundoff errors) the procedure was implemented with larger initial condition, which is slowly damped, if necessary, – even to numerical zero – as the computation goes on.

Having the real radial function $\mathrm{e}^{-\mathrm{i}\delta_\ell(k)} \chi_\ell(k, r)$, the condition (4.6) can be used to obtain a formula for the phase shift $\delta_\ell(k)$,

$$\tan\delta_\ell(k) = \frac{k\cos\phi_\ell - D\sin\phi_\ell}{k\sin\phi_\ell + D\cos\phi_\ell} , \qquad \phi = kr - \frac{\pi\ell}{2} ,$$

where D is the logarithmic mumerical derivative of the computed solution. The true phase of the solution is then $\exp(\mathrm{i}\delta_\ell)$.

The second and last step (apart from direct evaluation of ψ and β functions) is the multipole expansion of the two-electron potential

$$V(\mathbf{r}_1, \mathbf{r}_2) = \sum_{\lambda\mu} \frac{4\pi}{2\lambda + 1} \left(\frac{r_<^\lambda}{r_>^{\lambda+1}} - \frac{\delta_\ell^0}{r_2} \right) Y_{\lambda\mu}(\hat{\mathbf{r}}_1) Y_{\lambda\mu}^*(\hat{\mathbf{r}}_2) .$$

After angular integration one needs only to integrate three one-dimensional integrals and two two-dimensional integrals for every partial wave. The contributions of every next partial wave is compared to the sum of the previous and the computation terminates as soon as requested precision is achieved.

4.3 DWBA – second order

As will be shown in the "Results" part, the first-order distorted wave Born approximation yields better results than its plane-wave variant, but it still doesn't agree with convergent close-coupling computations from Aladdin. The formula (4.3) can be unwrapped further than just to (4.5). If one proceeds further to the next order in the Green's functions, it will be

$$T \approx T_2 = T_1 + DD + EE + (-1)^S (ED + DE) ,$$

where T_1 is defined above in (4.5) and the second-order corrections for electron colliding with hydrogen atom are [38]

$$DD = \frac{1}{2}\langle \chi_f^-(1)\psi_f(2)| \left[V - U_f(1)\right]\left[E - h_g\right]^{-1}\left[V - U_i(1)\right]\left|\psi_i(2)\chi_i(1)^+\right\rangle ,$$

$$DE = \frac{1}{2}\langle \chi_f^-(2)\psi_f(1)| \left[V - U_f(2)\right]\left[E - h_g\right]^{-1}\left[V - U_i(1)\right]\left|\psi_i(2)\chi_i(1)^+\right\rangle ,$$

$$ED = \frac{1}{2}\langle \chi_f^-(1)\psi_f(2)| \left[V - U_f(1)\right]\left[E - h_g\right]^{-1}\left[V - U_i(2)\right]\left|\psi_i(1)\chi_i(2)^+\right\rangle ,$$

$$EE = \frac{1}{2}\langle \chi_f^-(2)\psi_f(1)| \left[V - U_f(2)\right]\left[E - h_g\right]^{-1}\left[V - U_i(2)\right]\left|\psi_i(1)\chi_i(2)^+\right\rangle .$$

Indices in parentheses indicate on which particle's coordinates the respective variable depends. The two-electron potential V depends obviously on both the first and second electron and the S-wave proton field contribution depends on the same coordinate as the distorting potential which is subtracted above. Fro example, the first $[V - U_f(1)]$ bracket will evaluate to

$$\langle \mathbf{r}_1\mathbf{r}_2|(V - U_f(1))|\mathbf{r}_1\mathbf{r}_2\rangle = \sum_{\lambda\mu} \frac{4\pi}{2\lambda + 1} \left(\frac{r_<^\lambda}{r_>^{\lambda+1}} - \frac{\delta_\ell^0}{r_1} - \delta_\ell^0 U_f(r_1) \right) Y_{\lambda\mu}(\hat{\mathbf{r}}_1)Y_{\lambda\mu}^*(\hat{\mathbf{r}}_2) .$$

All functions above have been commented on except for the projectile Green functions $[E - h_g]^{-1}$. It can be expanded into a complete set of hydrogen states,

$$[E - h_g]^{-1} = \sum_n |n\rangle g_n^{(+)}\langle n| , \tag{4.8}$$

where the sum over intermediate state index n includes also integration over the continuous spectrum. In coordinate representation and in partial wave expansion the matrix element reads

$$g_n^{(+)}(\mathbf{r}', \mathbf{r}) = \frac{1}{k_n} \frac{1}{rr'} \sum_{l_n m_n} g_{l_n}^{(+)}(k_n, r', r) Y_{l_n m_n}^*(\hat{\mathbf{r}}')Y_{l_n m_n}^*(\hat{\mathbf{r}}) .$$

The energy $E_n = k_n^2/2$ is energy of the projectile decreased (or increased) by the difference of energy between the initial (i) and intermediate (n) atomic state.

$$E_{\text{tot}} = -\frac{1}{2n_i^2} + \frac{1}{2}k_i^2 = -\frac{1}{2n_n^2} + \frac{1}{2}k_n^2 = -\frac{1}{2n_f^2} + \frac{1}{2}k_f^2 .$$

The continuum intermediate states are the regular Coulomb functions

$$\psi_{L_n}(K_n, r) = \frac{4\pi}{K_n} \mathrm{i}^{L_n} \exp(\mathrm{i}\sigma_{L_n}) F_{L_n}(K_n, r) .$$

Capital letters designate quantum numbers belonging to the atomic electron. The phase σ_{L_n} is the Coulomb phase shift, but as the intermediate free states occur in (4.8) always in conjugated pairs, it will cancel.

The radial part of the Green's function partial wave can be computed as a product of a regular and irregular solution of (4.2) with correct boundary conditions,

$$g_{l_n}^{(+)}(k_n, r', r) = -\phi_{l_n}(k_n, r_<)\eta_{l_n}(k_n, r_>) \ ,$$

$$\phi_{l_n}(k, r) \propto \hat{j}_{l_n}(kr) + \mathrm{i}T_{l_n}\hat{h}_{l_n}^{(+)}(kr) \ , \qquad \eta_{l_n}(k, r) \propto \mathrm{i}\hat{h}_{l_n}^{(+)}(kr) \ .$$

The function ϕ has been computed in the same way as χ. The irregular function has been also computed using an initial value solver, but with inverted grid ($\delta < 0$), so that the "asymptotic" condition has been applied at the very beginning. Whereas the regular solution can be computed in real numbers (the equation (4.2) is real and the asymptotic phase in (4.6) doesn't depend on the coordinate and will thus hold for all radii), the complex phase of irregular solution will change with coordinate and the differential equation has to be split into its real and imaginary part, forming a set of two real differential equations. Moreover, when the solver approaches zero, it may have to follow divergent irregular functions, which significantly slows down the progress, as the adaptive steps have to be shortened. For both these reasons, computation of irregular solution of the distorting equation is by far the heaviest bottleneck of the whole code.

Distorting potential $U_g(r)$ used for computing these functions is a new arbitrary potential. It can be set to zero, which will produce a free particle Green's function, or computed using the intermediate wave functions. According to [38], the best agreement of theory and experiment is recovered if the Green's function distorting potential is computed between ground level states,

$$U_g(r_2) = \frac{1}{4\pi} \int \langle \psi_{1s}(\mathbf{r}_1)|V(\mathbf{r}_1, \mathbf{r}_2)|\psi_{1s}(\mathbf{r}_1)\rangle \mathrm{d}\Omega_2 \ ,$$

still its effect will be very small.

Having all the functions, the T-matrix contribution can be evaluated. For direct-direct term it is

$$DD = \frac{1}{2} \sum_n \left\langle \chi_f^{(-)}(\mathbf{r}_1')\psi_f(\mathbf{r}_2') \middle| (V - U_f(r_1'))\psi_n(\mathbf{r}_2')g_n^{(+)}(\mathbf{r}_1', \mathbf{r}_1)\psi_n^*(\mathbf{r}_2)(V - U_i(r_1)) \middle| \psi_i(\mathbf{r}_2)\chi_i^{(+)}(\mathbf{r}_1) \right\rangle ,$$

which can be straightforwardly modified to

$$DD = \frac{16\pi}{k_f k_n k_i} \sum_{\substack{n \\ l_i \lambda_1 l_n \lambda_2 l_i}} \mathrm{i}^{l_i - l_f} \frac{G_{\lambda_2 \mu_2 l_n m_n}^{L_n M_n} G_{L_i M_i \lambda_2 \mu_2}^{L_n M_n} G_{\lambda_1 \mu_1 l_f m_f}^{l_n m_n} G_{L_n M_n \lambda_1 \mu_1}^{L_f M_f}}{(2\lambda_1 + 1)(2\lambda_2 + 1)} I_{fni,L_n l_n}^{\lambda_1 \lambda_2} \frac{\sqrt{2l_i + 1}}{\sqrt{4\pi}} Y_{l_f m_f}(\hat{\mathbf{k}}_f) \ .$$

Gaunt's coefficients stand for angular integrations of $3Y$-integrals,

$$G_{l_1 m_1 l_2 m_2}^{LM} = \int Y_{l_1 m_1} Y_{l_2 m_2} Y_{LM}^* \mathrm{d}\Omega = \sqrt{\frac{(2l_1 + 1)(2l_2 + 1)}{4\pi(2L + 1)}}(l_1 m_1 l_2 m_2 | LM)(l_1 0 l_2 0 | L0) \ , \quad (4.9)$$

radial integral looks this way:

$$I_{fni,L_nl_n}^{\lambda_1\lambda_2} = \int\int \varphi_{fn,L_fL_n}^{\lambda_1}(r_1')\chi_{l_f}(k_f,r_1')g_{l_n}^{(+)}(k_n,r_1',r_1)\chi_{l_i}(k_i,r_1)\varphi_{ni,L_nL_i}^{\lambda_2}(r_1)\mathrm{d}r_1\mathrm{d}r_1' , \quad (4.10)$$

where

$$\varphi_{fn,L_fL_n}^{\lambda_1}(r_1') = \int \psi_{L_f}^*(f,r_2')\left(\frac{r_<'^{\lambda_1}}{r_>'^{\lambda_1+1}} - \frac{\delta_{\lambda_1}^0}{r_1'} - \delta_{\lambda_1}^0 U_f(r_1')\right)\psi_{L_n}(n,r_2')\mathrm{d}r_2' , \quad (4.11)$$

$$\varphi_{ni,L_nL_i}^{\lambda_2}(r_0) = \int \psi_{L_n}^*(n,r_2)\left(\frac{r_<^{\lambda_2}}{r_>^{\lambda_2+1}} - \frac{\delta_{\lambda_2}^0}{r_1} - \delta_{\lambda_2}^0 U_i(r_1)\right)\psi_{L_i}(i,r_2)\mathrm{d}r_2 . \quad (4.12)$$

Symbols "i", "n" and "f" in argument list of hydrogen radial functions stand for indication of energy, because the states can be both bound (energy dependent on N_i, N_n, N_f) and free (energy dependent on K_n). Summation over angular momenta projections m_i, m_f, m_n, μ_1 and μ_2 is removed in the formula for DD, because all projections are fixed by the choice $m_i = 0$ which, again, comes from the given orientation of $\mathbf{k}_i$ (i.e. along the z axis). All other m's are set by the Clebsh-Gordan coefficients in (4.9) from known M_i, M_n and M_f.

The other terms DE, ED and EE have a simillar pattern. They can be retrieved by exchanging ψ_i with χ_i resp. ψ_f with χ_f resp. doing both at once. The exchange must be done with all the indices as well, so that the change will be apparent also in the Gaunt's coefficients.

As the evaluation of the Green's function two-dimensional integral (4.10) containing other two one-dimensional integrals (4.11) and (4.12) in expressions for DD, DE, ED and EE is computationally expensive operation, a special care has to be given to the limits of summation. Though all possible values are allowed for l_i, l_f, l_n, λ_1 and λ_2, fortunately just some of the combinations will give nonzero Gaunt's coefficients. The angular momentum l_f is let to gradually increase and values of DD, DE, ED and EE are being stored separately for every partial wave (and checked for convergence). Due to the conservation of angular momentum and the rules for its composition, l_i will be always bounded by $l_f + L_i + L_f$. If it were larger, then not even the highest possible final composition $l_f + L_f$ would reach the lowest possible initial composition $l_i - L_i$. Manifestly, angular momentum wouldn't be conserved. Furthermore, parity has to be conserved, so only those l_i states that satisfy

$$(-1)^{L_i+l_i} = (-1)^{L_f+l_f}$$

will contribute. The same restrictions can be applied on the summation over Green's function partial waves l_n.

Atomic intermediate angular momenta are not restricted, so the summation over L_n is driven by convergence checking. But its value contributes to the bound for l_n as was just mentioned. For every L_n it is necessary to sum over all possible bound states and integrate over all free states. In reality, only several low lying bound states are taken in account.

Integration over free states is done by naive discretization of the allowed energy range (the intermediate free state energies cannot be arbitrary, because the initial total energy is not). To be precise, one ought to integrate even over the forbidden part of the spectrum. That involves solution of (4.2) with negative energy (imaginary wavenumber), so that instead of oscilating Riccati-Bessel functions we get their hyperbolical counterparts. As stated

in [38], their contribution quickly decays, so the forbidden region integration wasn't actually implemented here. The integration itself is just a summation with appropriate weights: The weight

$$\mathrm{d}k = 1$$

is used when summing a discrete state and the weight

$$w = \frac{\mathrm{d}E_n}{2k_n}$$

when the state is discrete. Why? We have chosen to sum energetically equidistant free states, whereas the original summation/integration in (4.8) runs over projectile (= Green's function) intermediate momenta. Thus the integration element has to be transformed and instead of $\mathrm{d}E_n$ we use, in Rydberg units,

$$\mathrm{d}k_n = \mathrm{d}\sqrt{E_n} = \frac{\mathrm{d}E_n}{2\sqrt{E_n}} = \frac{\mathrm{d}E_n}{2k_n} \ .$$

Interm. atomic state	Interm. atomic energy range	Green's function wavenumber
discrete bound	$-\frac{1}{2} < -\frac{1}{2N_n^2} < 0$	$k_n \in \mathbb{R}^+$
free allowed	$0 < \frac{K_n^2}{2} < E_{\mathrm{tot}}$	$k_n \in \mathbb{R}^+$
free forbidden	$E_{\mathrm{tot}} < \frac{K_n^2}{2} < \infty$	$k_n \in \mathbb{C}$

Table 4.1: Intermediate atomic states in the Green's function expansion.
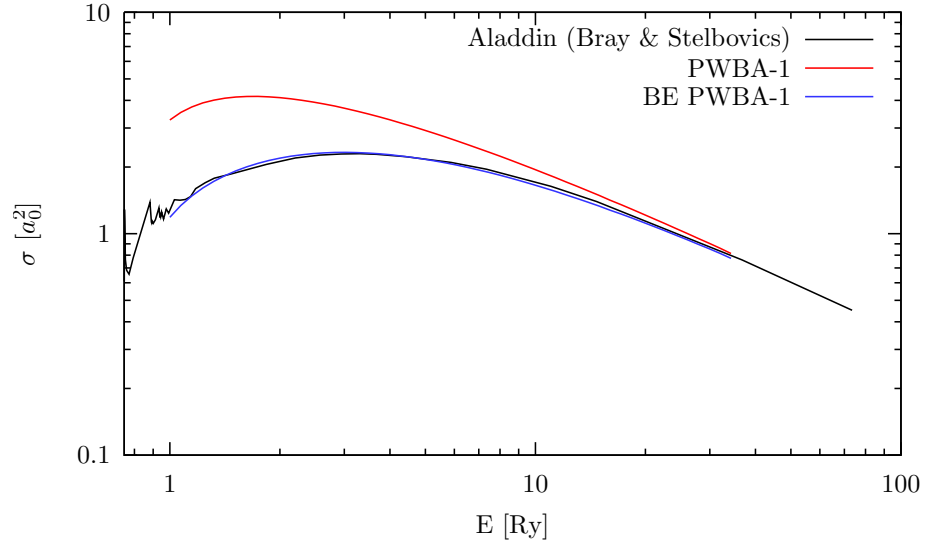
Fig. 4.1: Cross section for dipole-allowed excitation H(1s)→H(2p) at intermediate and high energies. The scaling parameters are $B = 1$ Ry (ionization energy) and $E = 0.75$ Ry (excitation energy).
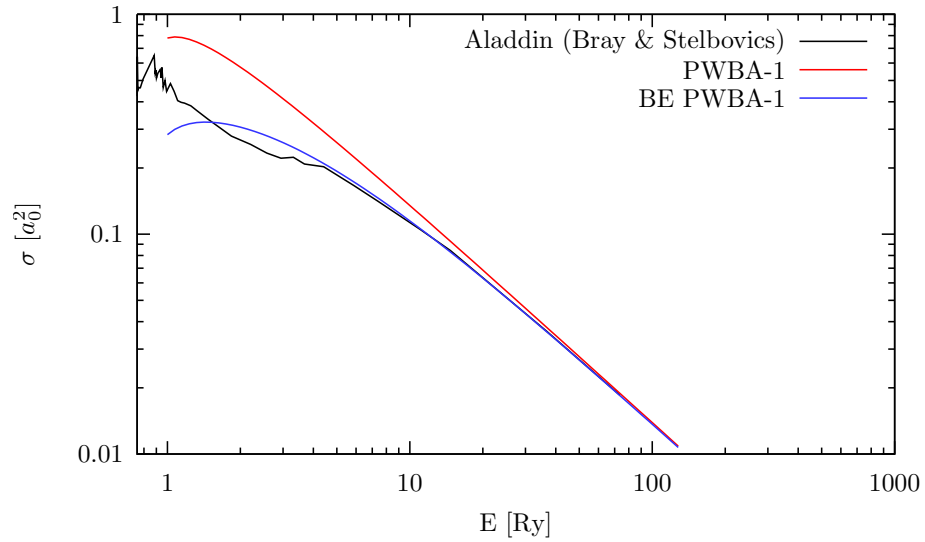
Fig. 4.2: Cross section for dipole-forbidden excitation H(1s)→H(2s) at intermediate and high energies. Intermediate region is approximated worse than in figure 4.1 above, because the indirect transition contribution is not included.

Chapter 5

Applications

One of aims of this work had been to create an easy-to-use computer program, that would produce all astrophysically relevant scattering data mentioned in the introduction. After thorough consideration, i.e. realization how time-expensive the exact computations can be, this aim has been slightly altered: to produce an intuitive programming interface (library), which would extract necessary data "on-the-fly", during execution of a derived work. The new task has thus been twofold:

- creation of a scattering data collection in a form that would be extensible by any new data and also somehow standardized for the ease of maintenance and

- creation of a set of routines usable by other computer codes that would retrieve the contents of the database according to the other code's needs.

For the first task, several representations have been considered: from already existing scattering data formats as for example the AMDIS format (see fig. 5.1) used by the Aladdin database to raw storage using text files with column data. The AMDIS files, though well established, are designed only for integral cross section data, which is a strong restriction. They might be used to store detailed scattering information (T-matrices) as well, but such modification discards the "standardization" which would prefer this particular format to raw text (or even binary) files, which are much more straightforward to parse.

Finally, to not completely reinvent the wheel, an existing format has been used, which has a strong support in information technology (including modern web browsers and operation systems): an *SQLite relational database* [39]. In a simplified way, a relational database is a set of tables containing the data, which can be interconnected among themselves by reference tables ("relations"). For present purpose the relations are irrelevant, but being a well spread technology, many tools are available for these databases. SQLite is one of the open-source implementations of the SQL standard (Structured Query Language) as well as a free command line program for manual database access. Graphical interfaces are also freely available. SQL allows fast and comfortable filtering, ordering and aggregation of the data and there is a C++ interface for SQLite, so that its inclusion in new software is really easy. For instance, for a given transition a legible short code can find out the highest available partial wave or retrieve all T-matrices.

There are several quantities that (with a varying completeness) describe the scattering event. Most of them can be computed with the knowledge of T_ℓ, which appear in the partial

```
Record-number            RN         12345
Theory-or-Experiment     TE         E
Method                   TA         BC
Element                  EL         Si
Ionic-STate              IST        +7
Initial-State            INS        Si +7
Final-State              FIS        Si +8
Final-Ion-Conf           CF
Data-Producer            PD
Transition-Energy        EN         303.87
OSC.Strength             OS
Number-of-Datapoints     ND         21
Org-E-EXP                SEE        1
Org-CS-EXP               CSS        A
Comment                  CM         test data
Ref-ID                   RI
#
Normalize-10-X           NRM10X     1
Normalize-10-Y           NRM10Y     -18
#
Data-Point-X             DTPNTX     200,298,323,347,372,386,396,421,
+445,470,494,519,544,593,642,740,789,888,986,1182,1363
Data-Point-Y             DTPNTY     0.019,0.004,0.127,0.298,0.355,
+0.397,0.500,0.522,0.662,0.642,0.756,0.781,0.826,0.860,0.877,
+0.917,0.878,0.952,0.890,0.821,0.812
#
Error-Range-X            ERRNGX
Error-Range-Y            ERRNGY     0.072,,0.047,,0.046,,0.033,,0.044,,
+0.065,,0.036,,0.045,,0.040,,0.037,,0.059,,0.067,,0.041,,0.067,,
+0.040,,0.055,,0.069,,0.056,,0.064,,0.057,,0.056,,0.056
#
!
```

Fig. 5.1: AMDIS cross section data file format (example shown for ionization of a quartz ion).

wave expansion of the T-matrix,

$$T = \sum_{\ell} Y_{\ell m_i - m_f}(\hat{\mathbf{k}}_f) T_\ell \ .$$

Here, as earlier in the text, the z-axis is oriented along the incoming projectile momentum, so that the spherical harmonic associated to k_i yields $\delta_{m_1 0}$, where m_1 is the third component of projectile angular momentum. Consequently, it is the partial T-matrix T_ℓ that has been used as the intermediate product of the computations that is to be stored in database, indexed by initial and final atomic quantum numbers, initial projectile energy, final partial wave angular momentum ℓ and global quantum numbers L and S.

The utility code (and associated standalone interface library) can then be used to produce the following information:

- the scattering amplitude

$$f_{i\to f}^S(E) = -\frac{1}{2\pi} T_{i\to f}^S(E) = -\frac{1}{2\pi} \sum_L f_{i\to f}^{LS}(E) = -\frac{1}{2\pi} \sum_{\ell L} Y_{\ell m_i - m_f}(\hat{\mathbf{k}}_f) T_{fi,\ell}^{LS}(E) \ ,$$

38

- the differential cross section

$$\frac{\mathrm{d}\sigma^S_{i\to f}}{\mathrm{d}\Omega}(E) = \frac{k_f}{k_i}\frac{2S+1}{4}|f^S_{i\to j}|^2 \ , \tag{5.1}$$

- the partial integral cross section

$$\sigma^{LS}_{i\to f}(E) = \frac{k_f}{k_i}\frac{2S+1}{4}\int_{4\pi}|f^{LS}_{i\to f}(E)|^2\mathrm{d}\Omega(\hat{\mathbf{k}}_f) = \frac{k_f}{k_i}\frac{2S+1}{16\pi^2}\sum_\ell |T^{LS}_{fi,\ell}(E)|^2 \ ,$$

- the "complete" integral cross section

$$\sigma_{i\to f}(E) = \sum_{LS}\sigma^{LS}_{i\to f}(E) \ , \tag{5.2}$$

- the total cross section

$$\sigma_i(E) = \sum_{n_f=1}^{\infty}\sum_{l_f=0}^{n_f-1}\sum_{m_f=-l_f}^{l_f}\sigma_{i\to f}(E) \ ,$$

- and also the momentum transfer

$$\eta^{LS}_{i\to f} = \int \frac{\mathrm{d}\sigma^{LS}_{i\to f}}{\mathrm{d}\Omega}(E)(1-\cos\vartheta)\mathrm{d}\Omega(\hat{\mathbf{k}}_f)$$

- or the dimensionless, $i\leftrightarrow j$ symmetrical, collision strength

$$\Omega^{LS}_{i\to f}(E) = k_i^2\sigma^{LS}_{i\to f}(E) \ . \tag{5.3}$$

Whenever one knows the cross section for the inelastic process $i\to j$, it can be used also to compute the cross section for a reverse process. According to the theorem of reciprocity [40], the matrix elements $T_{i\to j}$ and $T_{j\to i}$ are just the same, which results in the relation

$$p_i^2\sigma_{i\to j}(E_i) = p_j^2\sigma_{j\to i}(E_j) \tag{5.4}$$

meaning

$$(E_{\mathrm{tot}} - E_i^{\mathrm{at}})\,\sigma_{i\to j}(E_{\mathrm{tot}} - E_i^{\mathrm{at}}) = (E_{\mathrm{tot}} - E_j^{\mathrm{at}})\,\sigma_{j\to i}(E_{\mathrm{tot}} - E_j^{\mathrm{at}}) \ .$$

For this reason is the collision strength "$i\leftrightarrow j$ symmetrical".

Though the saved results are (within some precision) converged with respect to the grid length and allowed angular momenta, the energy mesh is obviously discrete and a user may generally want to retrieve a cross section value which has not been precomputed. In such cases, the values are interpolated from surrounding samples. Because the cross sections do contain sharp resonances, smooth interpolations are not adequate here. Thus, a simple linear interpolation has been used.

Together, the program package structure is described in figure 5.2. Computational units serve to produce scattering T-matrices in their respective validity range – exterior complex

scaling is used for low energies, Born-type approximations for higher energies. The T-matrices are produced in the form of SQL batch files, which can be comfortably inserted into existing databases by a single shell command[1]

```
# sqlite3 database.db < batch.sql
```

The user interface `hex-db` then extracts requested information from a given database file, for example by a call

```
# seq 0.01 0.01 3.14 | hex-db --database "hex.db"   \
                        --ni=1 --li=0 --mi=0  \
                        --nf=3 --lf=0 --mf=0  \
                        --S=0 --E=1.213 --dcs      > output-1s3s.dcs
```

which will print differential cross section for angles $0.01 \leq \vartheta \leq 3.14$ for H(1s) $\rightarrow$ H(3s) transition, total spin being zero, at $E = 16.5$ eV. A command line interface (CLI) has been chosen rather than full graphical user interface (GUI) to allow easy inclusion in Unix shell scripts. Detailed information on available command line arguments is given in the electronic attachment to this thesis.
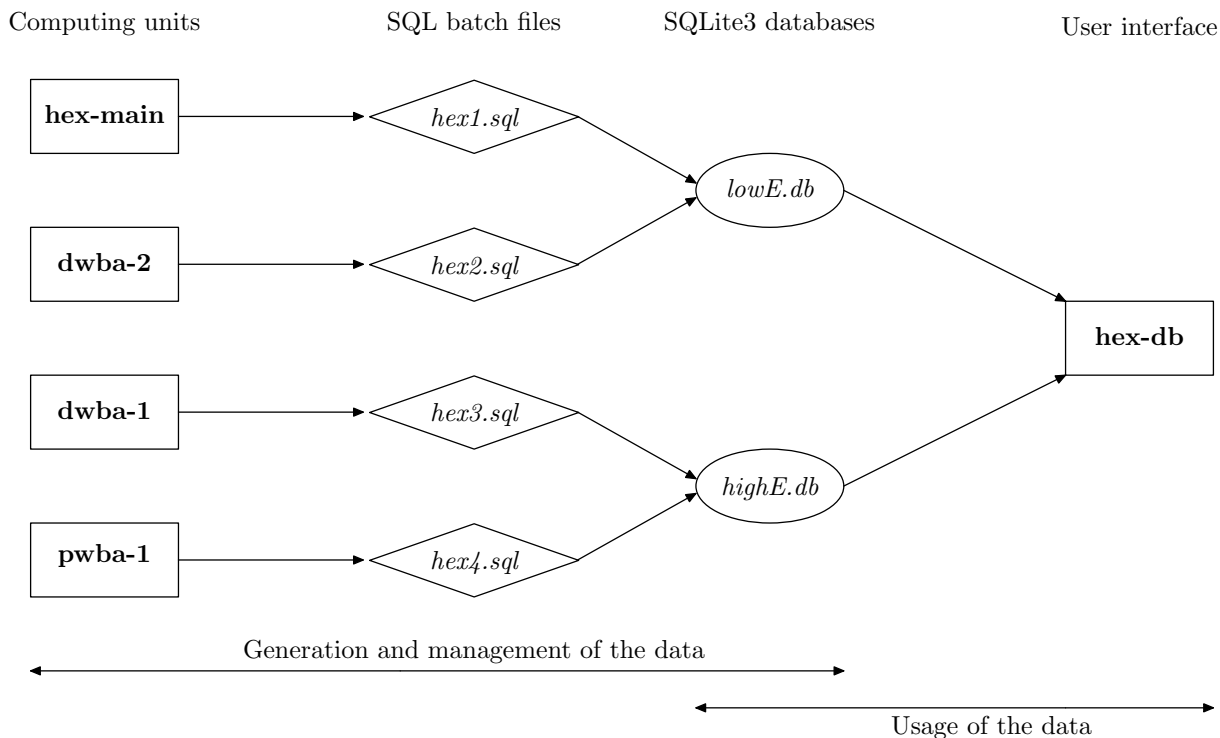
Fig. 5.2: Hex toolchain

---

[1]Standard Unix (Linux, CygWin, ...) shell is assumed; there is (yet) no version for Microsoft Windows operating system.

Chapter 6

Results

In this chapter the computed results are presented, together with comparison with other researchers' codes and/or with the experiment.

6.1 Exterior complex scaling

The complexity of the low-energy computations arises from omnipresent partial wave- and multipole expansions and the eventual convergence is understood mostly with respect to the angular momenta summations. Nevertheless, to have a solid ground on which to sum the partial contributions, one has to choose a proper grid, i.e. the spacing in the coordinate representation. For exterior complex scaling, three parameters from the figure 3.2 are crucial: the turning point R_0, marking the end of purely real grid, the θ_{ecs}, being the ECS rotation angle, and R_{max}, which is the trailing point of the grid discretization.

Far from the potential influence the outgoing wave function will be proportional to the free spherical wave

$$\psi_{\text{out}} \sim \frac{1}{r} e^{\mathrm{i} k_f \rho} \ .$$

As the radial coordinate possesses a positive imaginary part, ψ_{out} will exponentially decrease according to

$$\psi_{\text{out}} \sim \frac{1}{\rho} e^{\mathrm{i} k_f \operatorname{Re}\rho} e^{-k_f \operatorname{Im}\rho} = \frac{1}{\rho} e^{\mathrm{i} k_f \operatorname{Re}\rho} e^{-k_f (r - R_0) \sin \theta_{\text{ecs}}} \ .$$

Now, if we choose an integer n, we can see that ψ_{out} will be damped by the factor at least e^{-n} for all distances $r - R_0 \geq r_n$, where

$$r_n = \frac{n}{k_f \sin \theta_{\text{ecs}}} \ .$$

Apparently, for a given $\theta_{\text{ecs}} > 0$, there always exists a sufficient distance far from the atom, where the wave function will be damped under any limit. This can be used in the construction of an effective grid as explained below. In all calculations the angle θ_{ecs} has been fixed at $\frac{\pi}{5}$. Two numerical tests were done to verify that the results won't change with the change to $\frac{\pi}{4}$ or $\frac{\pi}{6}$.

We may choose an arbitrary n and θ_{ecs} such that a wave with the wavenumber k_f will be damped "just enough" for our numerical purposes after the distance r_n. Another wave with $k'_f = 2k_f$ is going to be damped twice faster whereas the wave with $k''_f = k_f/2$ twice slowlier.
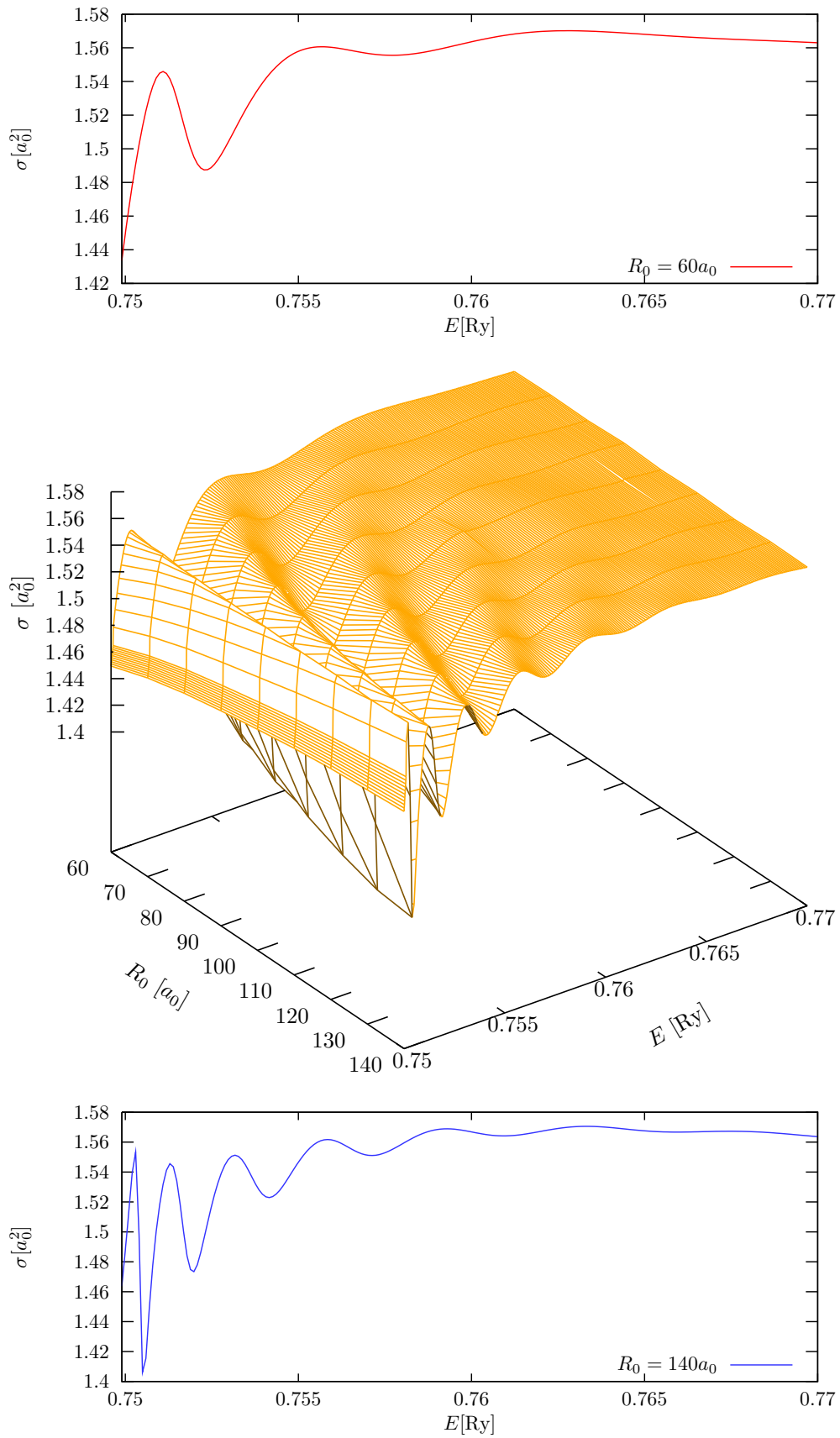
Fig. 6.1: R_0 convergence for elastic cross section just after the $n = 1 \rightarrow n = 2$ threshold.

In numerical calculations the "fast" waves (with large wavenumber) are mostly problematic. The discretized grid has to be fine enough to describe their quickly varying shape with satisfying presicion. For the real ECS grid the outcome is simple: the grid step must be approximately proportional to the inverse wavenumber (disregarding the proportionality constant). For high energies the storage requirements thus considerably grow.

The complex part of the coordinate has to be long enough to damp all waves with relevant energy. In a complicated system which can absorb some energy of the projectile (e.g. by excitation) the outgoing solutions present in the wavefunction ψ may have quite various energies. The grid thus ought to be long enough to damp the long wave part and at the same time fine enough to accurately describe rapidly oscilating short wave parts. These two requirements cannot be generally satisfied together due to the enormous computational cost. Fortunately, because the "fast" waves damp faster, the complexified grid can become coarser as r approaches R_{max}.

The mentioned discretization is valid not only for finite difference methods, but for finite elements methods as well. In the program Hex the B-spline set is used to expand the functions, but the idea is simillar. B-splines are defined by a (generally non-uniform) grid of knots and their shape is derived from distances between the knots: the further the two neighbouring points are, the slowlier the B-spline changes with distance.

A correct choice of R_0 and R_{max} is the first topic here to discuss. When the projectile impact energy is just slightly above an excitation threshold, the solution will contain the pair "excited atom + slowly outgoing projectile", which has a long-wave character in one of the coordinates. Consequently, with finite R_{max} we can expect in the cross section that the small regions just above the excitation thresholds may contain unphysical behaviour which originates from insufficiently damped outgoing long-wave solutions.

As an example of this phenomenon, the surrounding of the $n = 1 \rightarrow n = 2$ transition has been chosen. All angular momenta have been set to zero for simplicity – we scatter an S-wave on spherically symmetrical hydrogen 1s-state with disabled simultaneous intermediate transitions to other angular momentum states. The figure 6.1 represents integral cross section dependence on energy for several different R_0's from $60a_0$ to $140a_0$. The terminating distance R_{max} was always $R_0 + 40a_0$. The top (red) graph represents the cross section dependence for $R_0 = 60a_0$, $R_{max} = 100a_0$, the lower (blue) graph the dependence for $R_0 = 140a_0$, $R_{max} = 180a_0$ and the yellow surface plot in the middle shows the visualization of the gradual change between these two boundaries. It shows that with larger R_0 the shape is worse and worse. On the contrary, we would expect it to improve, as we are including more interparticle potential. However, with more interaction the resulting states are spatially larger and their non-harmonical part does fit less into the R_{max}-bounded space.

The same process is inquired in figure 6.2, now from the other end – the effect of R_{max}. Starting from the same configuration, $R_0 = 60a_0$, $R_{max} = 100a_0$, the complex part of the grid is scaled gradually up to $R_{max} = 220a_0$. The original strongly oscilatory nature improved into a smooth curve with a single unconverged defect just above the threshold.

Once we have a properly spaced grid, it is possible to undergo the actual calculation. By the convergence we now understand the convergence with respect to the angular momenta. There are three quantum numbers connected with angular momentum: L, l_1 and l_2 and all of them are necessarily limited in the actual calculation. The main output of the computer code are the integral cross sections, so the summation in (5.2) is considered the outermost expansion and the convergence is analyzed with respect to L. The program Hex has to be
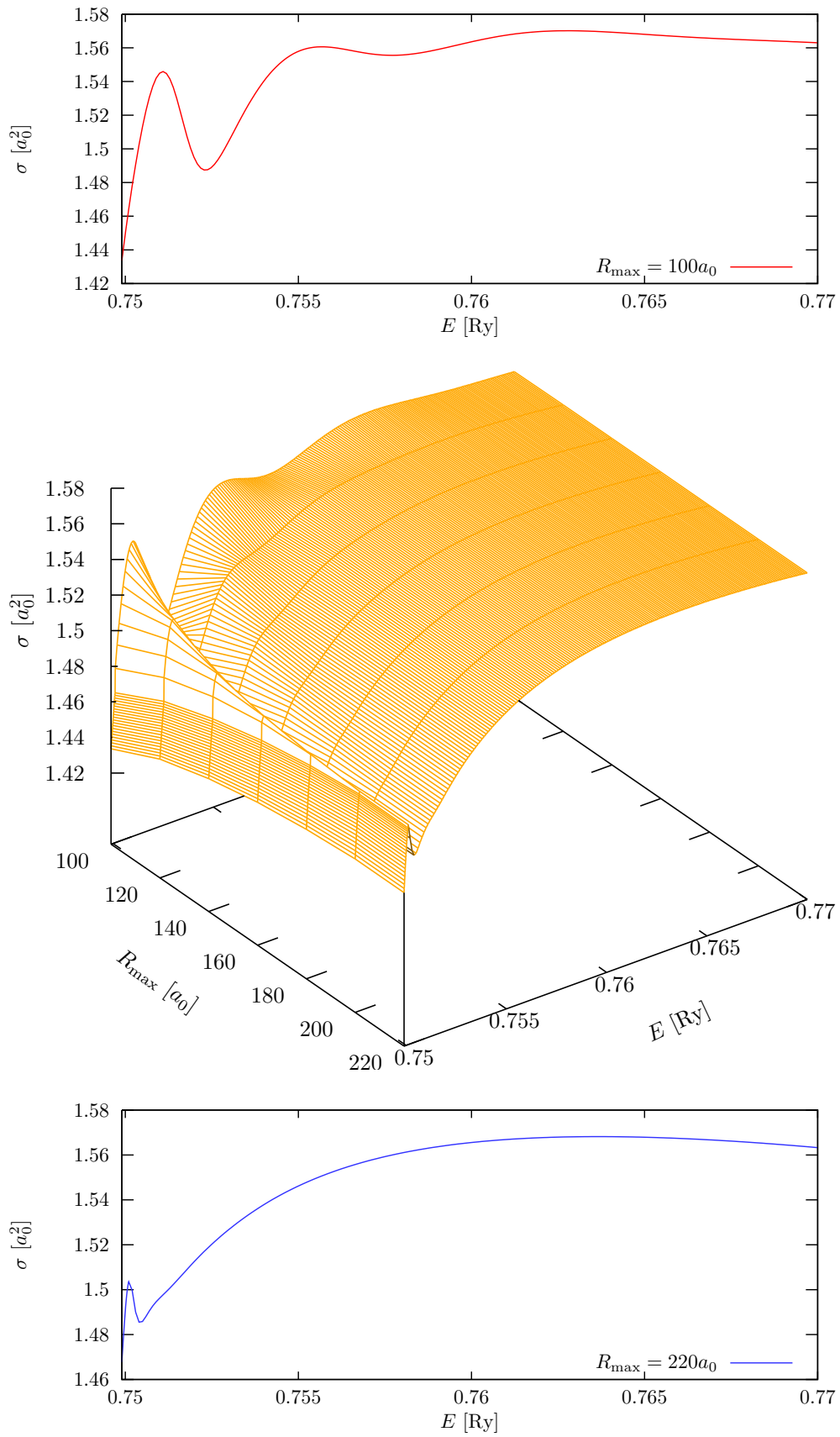
Fig. 6.2: $R_{\max}$ convergence for elastic cross section just after the $n = 1 \to n = 2$ threshold.
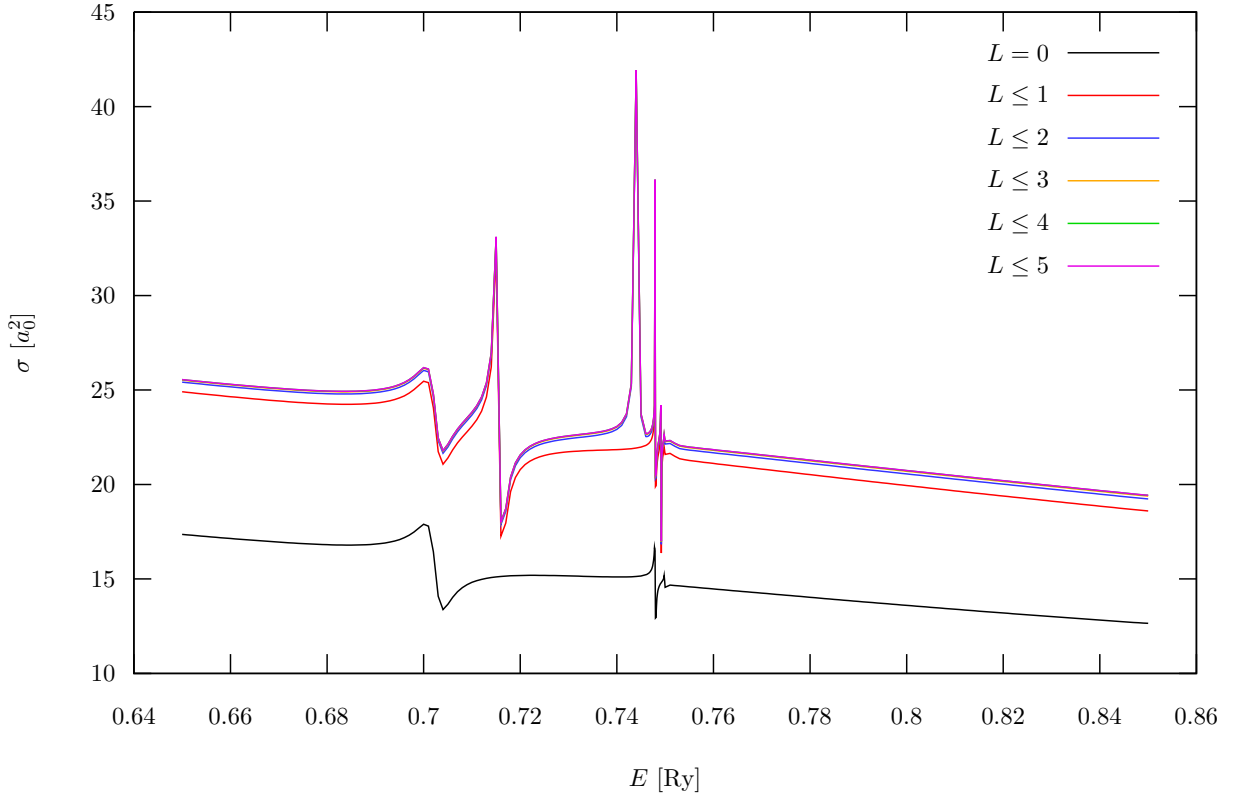
**Fig. 6.4:** Partial wave convergence for elastic $1s \to 1s$ scattering in the vicinity of first excitation ($n = 1 \to n = 2$) threshold, which is at the energy $E = 0.75$ Ry.

run for every L and S separately. The necessary numerical restriction on l_1 and l_2 (which determine the block structure of most matrices) are then constraints on angular momenta of individual electrons, which have to compose the total angular momentum.

For example, a restriction "$\max l = 0$" is allowable when computing $^1S^e$ wave ($S = 0, L = 0$), but cannot result in nonzero cross section for any higher terms. Moreover, all resonances that would require one of these electrons to have a higher angular momentum than 0 are inaccessible. This may not be a drawback for sufficiently low energies where the resonances do not occur, but still the restrictions on l_i need to allow at least the specified initial and final state (in mentioned hypothetical case it would not be possible to start e.g. with 2p state). However, the larger values of l_i are used, the more converged will be the result, see the figure 6.3.

The importance of higher partial
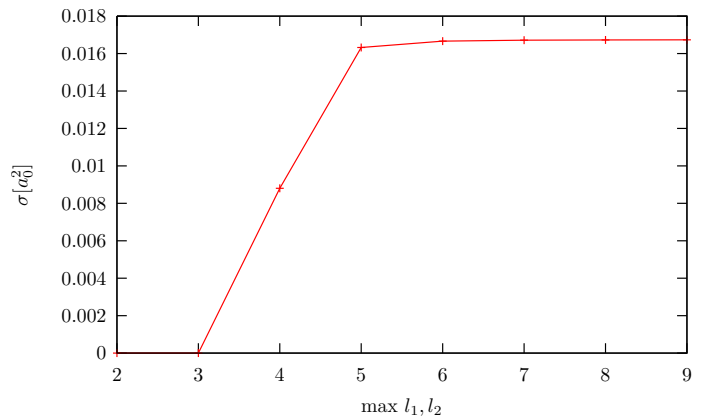
Fig. 6.3: Convergence of elastic integral cross section of $^1G^e$ partial wave ($L = 4$) at the energy of 16.5 eV. The restrictions $l_{1,2} \le 4$ would give approximately half of the converged cross section.

waves increases with impact energy. Integral cross section for the familiar region around the $n = 1 \rightarrow n = 2$ excitation threshold is plotted in the figure 6.4 for contributions taken from one up to six partial waves. We can see that inclusion of already three partial waves gives final shape, at least further from the threshold, where no more resonances may arise in higher partial waves. The situation is more complicated at higher energies – around ionization threshold and onward. The three left graphs of figure 6.5 show simillar convergence study of 1s $\rightarrow$ 3s, 3p and 3d excitation, this time in the differential cross section. We can clearly see that even after inclusion of five partial wave contributions the shape is not fixed.

When all contributions sum together, Hex output can be tested against the experiment. Atomic hydrogen is unfortunately a difficult element for scattering measurements, because the natural state of hydrogen is a diatomic molecule and keeping the atoms separated requires strong UV radiation which might influence the results. There exists just one larger measurement of integral cross section, for excitation to 2s and 2p, see figures 6.6, 6.7. Other published results are only for differential cross section.

6.2   Born approximation

For high energies a simple first-order Born approximation has been used here with the intention to compare its results with the (hopefully) better results of the distorted wave Born approximation. The Born approximation (disregarding the exchange effects) results in the formula for scattering amplitude [2]

$$f = -\frac{1}{2\pi}\langle\Psi_{\text{out}}|\hat{H}_{\text{int}}|\Psi_{\text{inc}}\rangle.$$
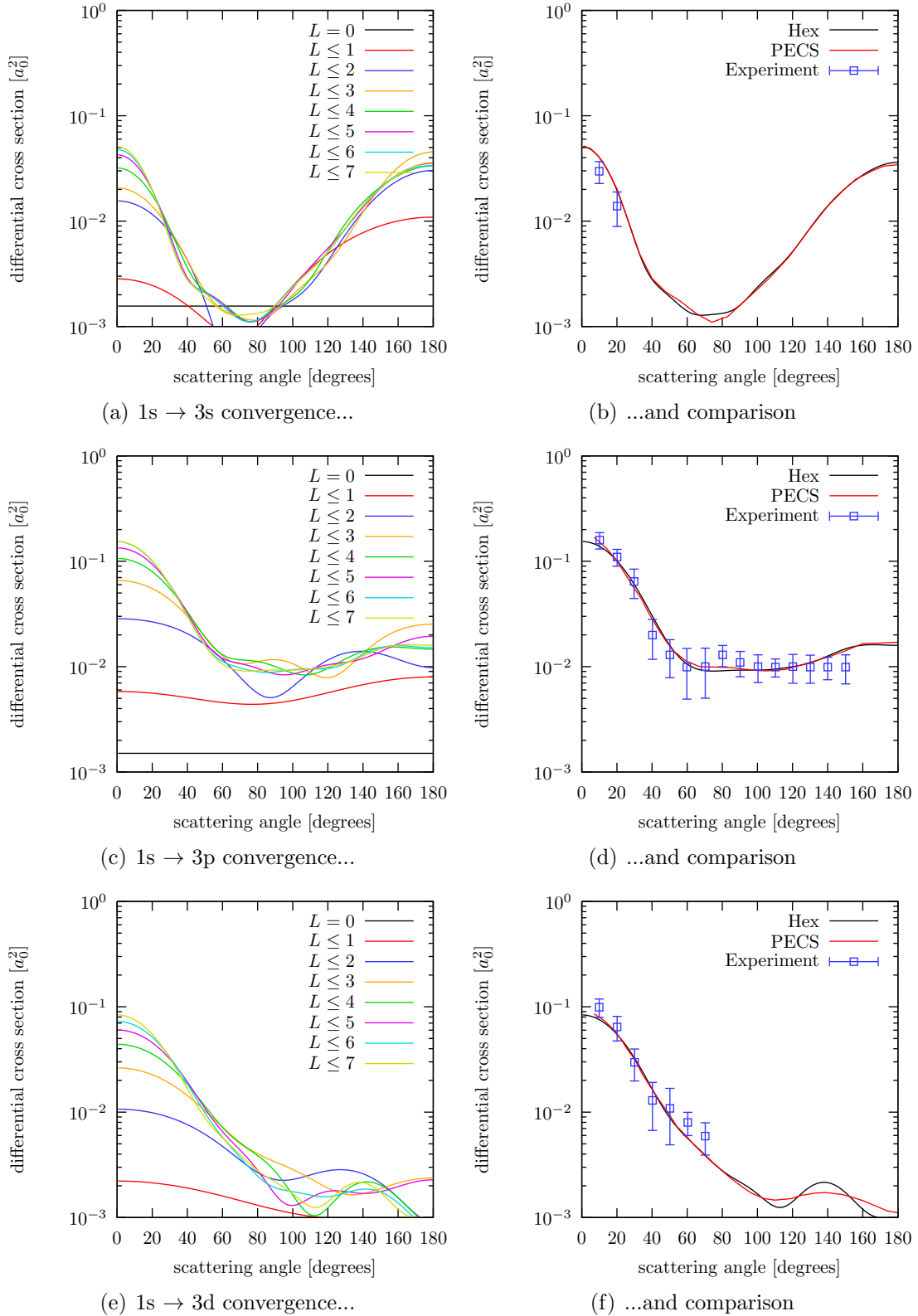
Here, both Ψ_{inc} and Ψ_{out} are then expanded in partial waves according to (3.6) and the matrix element is computed for a sufficient amount of summation terms. The necessary number of these angular momentum terms increases with energy and with orbital quantum number of both the initial and final atomic state. Some characteristic trends are presented in figures 6.8 and 6.9.

As pointed out in the fourth chapter, even this simple first-order plane wave calculations can lead to very good results when the BE scaling is applied. A quick look at graphs 4.1 and 4.2 reveals that BE-scaled first-order plane wave cross sections coincide with the convergent close coupling calculations for energies greater that approximately $E = 10$ Ry.

Unfortunately, there is no such mechanism that would transform T-matrices and all derived variables, so for a general usage a better method is still necessary. And also the differential cross section has to be computed in some other way, because – scaled or not – Born-type cross section is known to have a wrong angular dependence.

## 6.3   Distorted wave Born approximation

The distortion of a plane wave should – at least partially – account for physical distortion by the atomic potential. When a first order is taken, the results can improve like in the case of elastic scattering as shown in the figure 6.10. We can see that the first order of distorted wave Born approximation follows more closely the convergent close-coupling computation by Bray and Stelbovics than the simple plane wave Born approximation. However, in some

(a) 1s → 3s convergence...

(b) ...and comparison

(c) 1s → 3p convergence...

(d) ...and comparison

(e) 1s → 3d convergence...

(f) ...and comparison

Fig. 6.5: Differential cross section for 1s → 3s, 3p, 3d transtitions at $E = 16.5\,\mathrm{eV}$. Convergence with respect to the total angular momentum partial waves shown on left lanels, comparison with PECS calculation of Bartlett [21] and the measurement of Williams [42] on right panels.
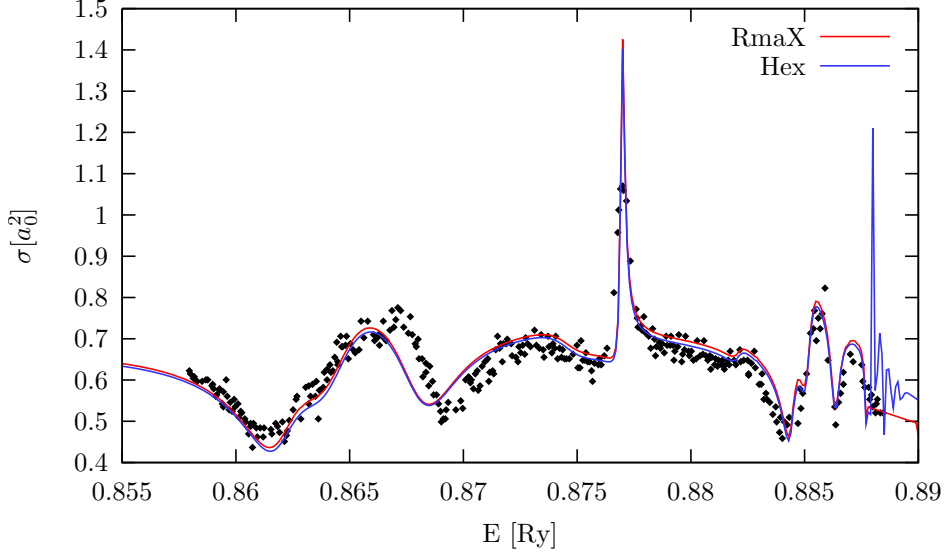
Fig. 6.6: Comparison of theoretical predictions for inelastic cross section (1s→2s transition), as produced by RmaX and Hex. Experimental data are by Williams [42]. Though both theories give similar results, the experimental data show a deviation around $E = 0.867$ Ry. The surrounding of $E = 0.889$ Ry is flat with RmaX, because of the numerical method employed in the asymptotic region, see [43]. The skipped interval around a resonance can be shrunk at the expense of computational resources.
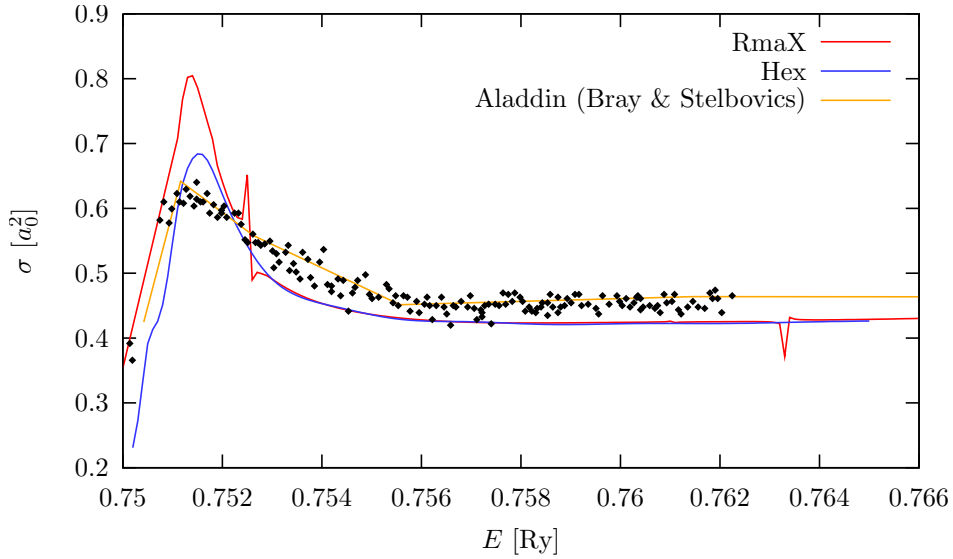

Fig. 6.7: Same as above, for energies just above the excitation threshold. The major structure in this figure and also the main source of disagreement between the codes in this figure is the $H^-(2s2p)\ ^1P^o$ shape resonance with the centre at $E_r = 0.75128(5)$ Ry and halfwidth of $\Gamma/2 = 0.00069(5)$ Ry. [44] Nevertheless, none of them fits to experimental data. Note the pseudo-resonances produced by RmaX: First one is in $^3P^o$ partial wave at 10.235 eV, the second in $^1S^e$ partial wave at 10.38 eV; neither one is tabulated in literature.
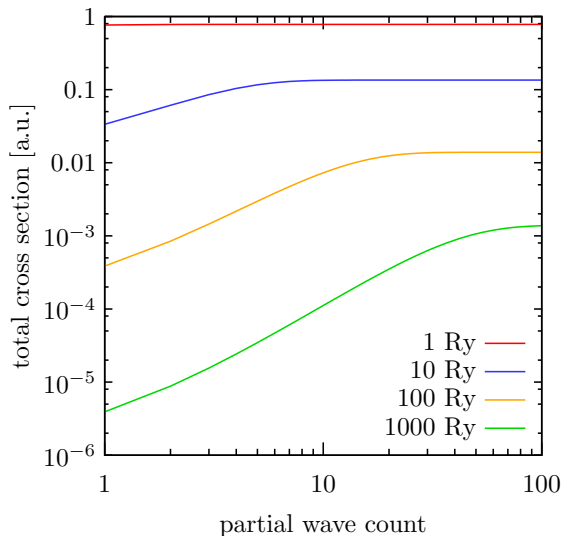
Fig. 6.8: Convergence of cross section for 1s→2s transition.
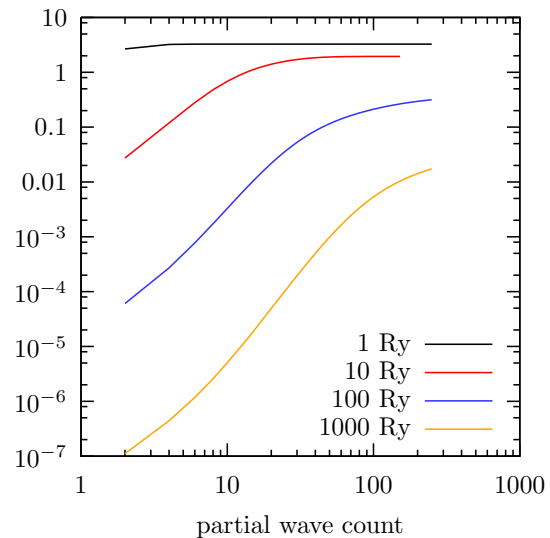
Fig. 6.9: Convergence of cross section for 1s→2p transition. Note the ten times higher average partial wave count than in 6.8.

other transitions where higher orders are important (or the distorted wave Born series does not converge well) the results may be actually worse than with PWBA-1, which is illustrated in the figure 6.11 for excitation H(1s)→H(2s).

Still, even though the integral cross section deviates strongly in H(1s)→H(2s) process, the differential cross section computed using the DWBA-1 method has better shape than with simple plane waves, fig. 6.13. Other differential cross sections for high energy scattering are presented in figures 6.12 and 6.14.

By inspection of the integral cross section graphs, we can conclude that the distorsion is negligible for fast electrons, with kinetic energies above 1 keV, due to the fact that the encounter is too short for the distortion to arise and manifest itself. Consequently, for energies above ∼1 keV DWBA-1 and PWBA-1 results match very well and the latter can be used.

Observing the differential cross sections, it seems that plane wave Born approximation and distorted wave Born approximation agree on the forward peak, at least in the first order. On the contrary, the backward directions differ substantially. DWBA-1 goes generally more closely to the experimental data. A natural conclusion can be that the first-order distorting effects do have an observable impact on the final cross section. On the other hand they still do not represent the scattering event within the experimental error. In the intermediate energy regime a higher-order method is necessary. Second order of the DWB approximation has been implemented, but the calculation is time demanding and its converged results have not been assembled in time for inclusion in this text.

From dramatic improvement of differential cross section of DWBA-1 over PWBA-1 one could guess that converged results of DWBA-2 ought to satisfactorily connect to the low-energy results of Hex. This connection is yet to be investigated as soon as necessary computational resources are available.
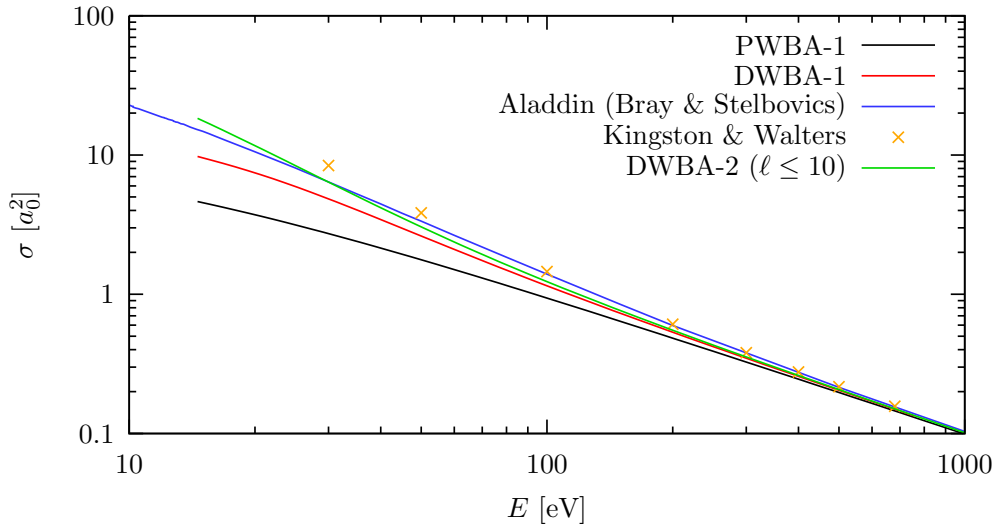
Fig. 6.10: High-energy cross sections for elastic scattering on H(1s). Distorted wave Born approximation gives better agreement with convergent close-coupling computation from Aladdin database. Even better, still, is the second order computation of Kingston and Walters [45], which has been the main motivation for general implementation of DWBA-2. Not-yet-converged results of author's implementation of DWBA-2 are presented in green colour.
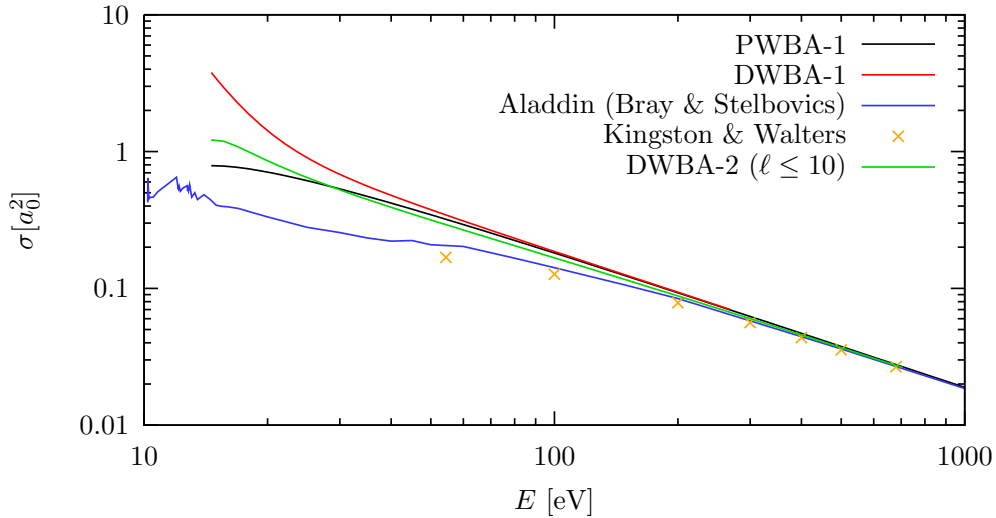

Fig. 6.11: High-energy cross sections for inelastic transition H(1s)→H(2s). The first order of distorted wave Born approximation gives wrong correction to the plane wave approximation. The reason may arise in imperfect description of intermediate 1s→2p→2s transition.
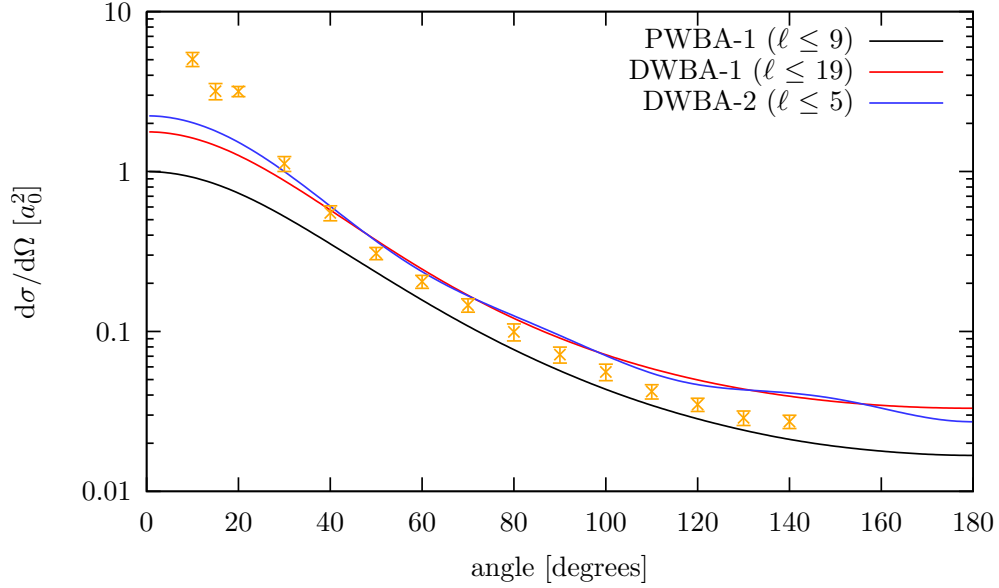
Fig. 6.12: Differential cross section of elastic scattetin on H(1s) ar the energy of $E = 50$ eV. Experimental data come from Williams [46] and apparently doo not agree with any method. DWBA-1 as computed by the present author precisely matches the output of the program by Bartschat [35]. The DWBA-2 calculation, though, has been summed just from five partial waves, so it may not be well converged.
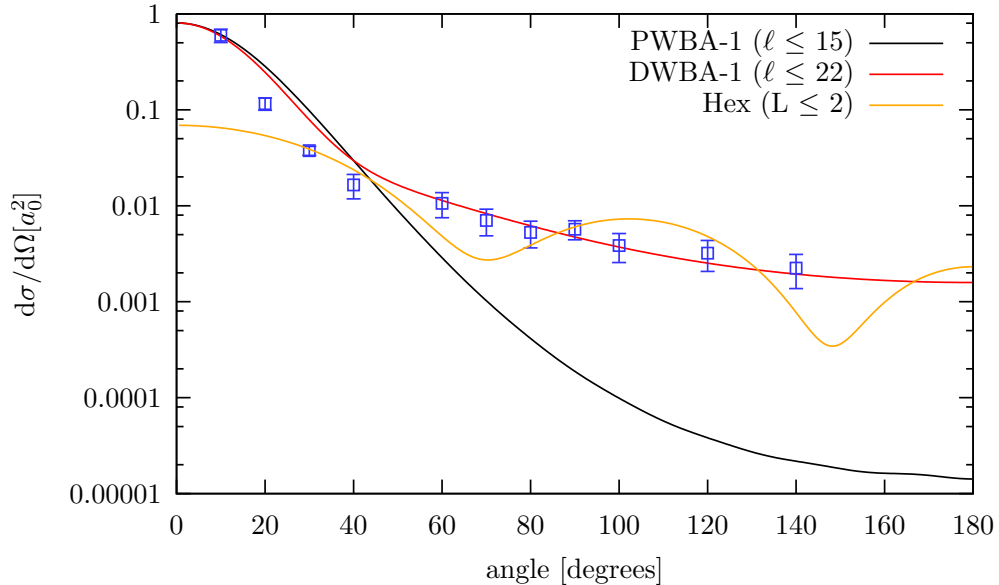
Fig. 6.13: Differential cross section of H(1s)→H(2s) excitation at the energy of $E = 4$ Ry. DWBA-1 results follow well the Aladdin data. The program Hex has been also included into this comparison, though with three partial waves the results are not fully converged. Nevertheless, it oscillates along the correct values. Experimental data are from [46].
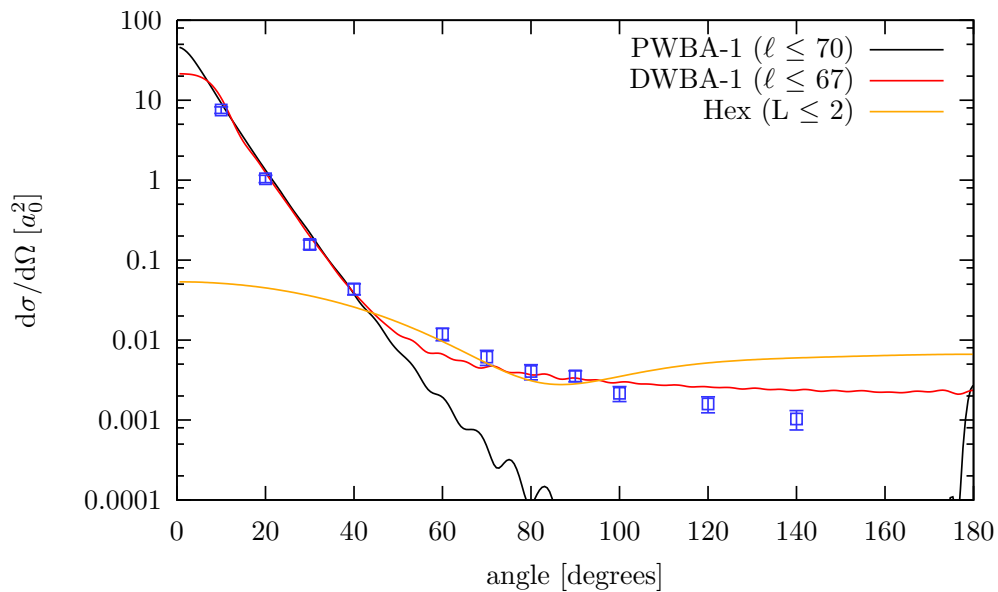
Fig. 6.14: Differential cross section of H(1s)→H(2p) excitation at the energy of $E = 4\,\text{Ry}$. DWBA-1 results are again closest to the database. For transitions changing angular momentum of the atomic electron a vast number of partial waves is needed. The rapid oscillations of PWBA-1 curve prove insufficient convergence even after summing 70 partial waves. Experimental data are from [46].

Chapter 7

Conclusion

Research fields – astronomy and plasma physics – that use electron-hydrogen scattering data as an input to their models feel the need for more detailed and in some sense canonical databases. Presently, there are several freely accessible on-line databases, like e.g. Aladdin; nevertheless, their data either are not complete or they contradict themselves. Likewise, several computer programs have been published that compute scattering cross sections and other related variables, but – similarly – they either use a "narrow method", meaning that the validity does not span a wide energy range, or they do not match with other programs and / or the experiment.

For these reasons an attempt was made in this thesis (and is supposed to continue in author's further research) to provide a unified user interface, that would output valid cross sections etc. for all possible energies and electron-hydrogen collisional processes.

A set of computer programs has been created for various energy domains. Low energies (i.e. with projectile kinetic energy below or just a few eVs above the ionization threshold) are covered by an exterior complex scaling based precise solution of Schrödinger equation in the B-spline basis. The resulting program Hex has been shown to produce results well matching the experiment and in some cases doing even better than already published R-matrix codes.

High energies have been solved using perturbation approaches: first-order plane wave Born approximation, first-order distorted wave Born approximation and second-order distorted wave Born approximation. The implementations had not been finished (or optimized) by the time of finishing this text. Still, it was possible to conclude that these are truly valid only asymptotically and in the intermediate region 1 Ry to 100 Ry their results deviate from experiment and other more reliable calculations. As a possibly best move, usage of the convergent close coupling method can be suggested, which consistently gives the best results for energies above the ionization threshold.

Besides the computational units (hex, pwba, dwba) a command line user interface (hex-db) has been created, which on request extracts needed intermediate results (scattering T-matrices) of the computational units from unified intermediate storage (an SQLite database file) and from them computes various other derived scattering variables like differential or integral cross sections, collision strengths or momentum transfer.

All programs together with their source codes and documentation are in the electronical attachment to this work.

Bibliography

[1] Ott W. R., Kaupilla W. E., Fite W. L.: *Polarization of Lyman-α radiation emitted in electron collisions with hydrogen atoms and molecules*, Phys. Rev. A **1** (1970) 1089–1098.

[2] Benda J.: *Srážky elektronů s atomy vodíku v astrofyzice*, Bc. Thesis, Charles university in Prague 2010.

[3] Anderson H., Ballance C. P., Badnell N. R., Summers H., P., *An R-matrix with pseudostate approach to the electron-impact excitation of H I for diagnostic applications in fusion plasmas*, J. Phys. B: A. Mol. Opt. Phys. **33** (2000) 1255–1262.

[4] International Atomic Energy Agency: *Aladdin* database at http://www-amdis.iaea.org/infoaladdin.php (accessed 25. 7. 2012).

[5] Bray I., Stelbovics A. T.: *Calculation of electron scattering on hydrogenic targets*, Adv. At. Mol. Opt. Phys. **35** (1995) 209–254.

[6] Janev R. K., Smith J. J.: *Atomic and plasma-material interaction data for fusion*, being a supplement to Nuclear Fusion **4** (1993).

[7] NIST *Electron-impact cross sections for ionization and excitation* database at http://www.nist.gov/pml/data/ionization/index.cfm (accessed 25. 7. 2012).

[8] Stone P. M., Kim Y.-K., Desclaux J. P.: *Electron-impact cross sections for dipole- and spin-allowed excitations of hydrogen, helium, and lithium*, J. Res. Natl. Inst. Stand. Technol. **107** (2002) 327.

[9] Yong-Ki Kim: *Scaling of plane-wave Born cross sections for electron-impact excitation of neutral atoms*, Phys. Rev. A **64**, 032713 (2001).

[10] I. Bray and Y. Ralchenko, http://atom.curtin.edu.au/CCC-WWW/ (data used as of 2001).

[11] Sweeney C. J., Grafe A., Shyn T. W., Phys. Rev. A **64** (2001) 032704.

[12] Salvat F., Jablonski A., Powell C. J.: **ELSEPA** – *Dirac partial-wave calculation of elastic scattering of electrons and positrons by atoms, positive ions and molecules*, Comp. Phys. Comm. **165** (2005) 157–190.

[13] Chinese atomic and molecular database, http://www.camdb.ac.cn/e/ (accessed 4. 4. 2012)

[14] The ADAS project, http://open.adas.ac.uk/ (accessed 4. 4. 2012)

[15] Janev R. K. *et al*: *Elementary processes in hydrogen-helium plasmas*, chapter I, Springer 1987.

[16] Schultz G. J.: *Resonances in electron impact on atoms*, Rev. Mod. Phys. **45** (1973) 378–422.

[17] Bylicki M., Nicolaides C. A.: *Theoretical resolution of the H^- resonance spectrum up to the $n = 5$ threshold: States of $^3P^o$ symmetry*, Phys. Rev. A **65** (2001) 012504.

[18] Bürgers A., Lindroth E.: *Doubly excited states in the negative hydrogen ion*, Eur. Phys. J. D **10** (2000) 327–340.

[19] Biaye M. *et al*: *The doubly excited states description of the negative hydrogen ion using special forms of the Hylleraas type wave functions*, Chin. J. Phys. **47** (2009) 166–172.

[20] Descouvemont P., Baye D.: *The R-matrix theory*, Rep. Prog. Phys. **73** (2010) 036301.

[21] Bartlett P. L.: *A complete numerical approach to electron–hydrogen collisions*, J. Phys. B: At. Mol. Opt. Phys. **39** (2006) R379–R424.

[22] McCurdy C. W., Martín F.: *Implementation of exterior complex scaling in B-splines to solve atomic and molecular collision problems*, J. Phys. B: At. Mol. Opt. Phys. **37** (2004) 917–936.

[23] Schenk O., Gärtner K.: *Solving unsymmetric sparse systems of linear equations with PARDISO*, Future Generation Computer Systems **20** (2004) 475–487.

[24] Davis T.: *Algorithm 832:* **UMFPACK***, an unsymmetric-pattern multifrontal method*, ACM Transactions on Mathematical Software **30** (2004) 196–199.

[25] Barrett R. *et al*: *Templates for the solution of linear systems: Building blocks for iterative methods*, 2$^\text{nd}$ ed., p. 13, SIAM, Philadelphia PA 1994.

[26] Zatsarinny O.: **BSR***: B-spline atomic R-matrix codes*, Comp. Phys. Comm. **174** (2006) 273–365.

[27] Callaway J.: *Electron-impact excitation of hydrogen atoms: Energies between the $n = 3$ and $n = 4$ thresholds*, Phys. Rev. A 37 (1988) 3692—3696.

[28] Scott N. S. *et al*: **2DRMP***: A suite of two-dimensional R-matrix propagation codes*, Comp. Phys. Comm. **180** (2009) 2424-2449.

[29] Fortin P. *et al*: *Deployment on GPUs of an application in computational atomic physics*, IEEE International Parallel & Distributed Processing Symposium, Anchorage AK, USA (2011).

[30] UK APAP network, http://amdpp.phys.strath.ac.uk/UK_RmaX/codes.html (accessed 2. 8. 2012).

[31] Berrington K. A., Eissner W. B., Norrington P. H.: *RMATRX1: Belfast atomic R-matrix codes*, Comp. Phys. Comm. **92** (1995) 290–420.

[32] Bartschat K., Bray I., Burke P. G., Scott M. P.: *Benchmark calculations for e-H scattering between the $n = 2$ and $n = 3$ thresholds*, J. Phys. B: At. Mol. Opt. Phys. **29** (1996) 5493–5503.

[33] Schultz D. R., Reinhold C. O.: *Elastic – Elastic scattering of electrons from atoms and ions*, Comp. Phys. Comm. **114** (1998) 342–355.

[34] Mansky E. J., Flannery M. R.: *The multichannel eikonal theory program for electron-atom scattering*, Comp. Phys. Comm. **88** (1995) 249–277.

[35] Madison D. H., Bartschat K.: *The distorted-wave method for elastic scattering and atomic excitation*, being the fourth chapter of *Computational atomic physics*, p. 65, Springer-Verlag Berlin Heidelberg, 1996, ISBN 3-540-60179-1.

[36] Flannery M. R.: *Elastic scattering: Classical, quantal and semiclassical*, being the 45th chapter of *Springer handbook of at., mol. and opt. physics*, p. 659, Springer Science+Bussiness Media, 2006, ISBN 0-387-20802-X.

[37] O_2scl library, http://o2scl.sourceforge.net/, (accessed 2. 8. 2012).

[38] Madison D. H., Bray I., McCarthy I. E.: *Exact second-order distorted wave calculation for hydrogen including second-order exchange*, J. Phys. B: At. Mol. Phys. **24** (1991) 3861–3888.

[39] Owens M.: *The definitive guide to SQLite* (2nd ed.), Apress, 2006, p. 368, ISBN 1-59059-673-0.

[40] Formánek J.: *Úvod do kvantové teorie II.*, p. 660, Academia, Praha 2004, ISBN 80-200-1176-5.

[41] Beck R. *et al*: *Galactic magnetism: Recent developments and perspectives*, Annu. Rev. Astron. Astrophys. **34** (1996) 155–206.

[42] Williams J. F.: *Resonance structure in inelastic scattering of electrons from atomic hydrogen*, J. Phys. B: At. Mol. Opt. Phys. **21** (1988) 2107–2116.

[43] Badnell N. R.: *A perturbative approach to the coupled outer-region equations for the electron-impact excitation of neutral atoms*, J. Phys. B.: At. Mol. Opt. Phys. **32** (1999) 5583–5591.

[44] Ho Y. K., Bhatia A. K.: *Doubly excited shape resonances in H^-*, Phys. Rev. A **48** (1993) 3720–3724.

[45] Kingston A. E., Walters H. R. J.: *Electron scattering by atomic hydrogen: the distorted wave Born approximation*, J. Phys. B: At. Mol. Phys. **13** (1980) 4633-4662.

[46] Williams J. F.: *Electron-photon angular correlations from the electron impact excitation of the 2s and 2p electronic configurations of atomic hydrogen*, J. Phys. B.: At. Mol. Phys. **14** (1981) 1197–1217.